

NACA RM E53J09

6845



2011 LIBRARY KAFB, NM
0143283

RESEARCH MEMORANDUM

FORCE, MOMENT, AND PRESSURE CHARACTERISTICS
OF SEVERAL ANNULAR NOSE INLETS
AT MACH NUMBER 3.85

By James F. Connors and Richard R. Woollett

Lewis Flight Propulsion Laboratory
Cleveland, Ohio ~~Unclassified~~

NASA Tech Pub Announcement #7

By IF AND

14/ Apr. 60.....

NK

GRADE or OFFICER MAKING CHANGE)

15 Feb. 61

CLASSIFIED DOCUMENT

DATE _____
This material contains information affecting the National Defense of the United States within the meaning of the espionage laws, Title 18, U.S.C., Secs. 793 and 794, the transmission or revelation of which in any manner to an unauthorized person is prohibited by law.

**NATIONAL ADVISORY COMMITTEE
FOR AERONAUTICS**

WASHINGTON

February 3, 1954

CONFIDENTIAL



NATIONAL ADVISORY COMMITTEE FOR AERONAUTICS

RESEARCH MEMORANDUMFORCE, MOMENT, AND PRESSURE CHARACTERISTICS OF SEVERAL ANNULAR
NOSE INLETS AT MACH NUMBER 3.85

By James F. Connors and Richard R. Woollett

SUMMARY

An investigation to evaluate the over-all performance characteristics of several annular nose inlets was conducted in the Lewis 2- by 2-foot supersonic wind tunnel at a Mach number of 3.85. The four experimental configurations consisted of a one-cone, a one-cone (low-angle cowl), a two-cone, and an isentropic inlet. Over an angle-of-attack range from 0° to 9° , complete pressure and three-component force data were recorded.

For application in a hypothetical ram-jet engine at zero angle of attack, the isentropic inlet indicated the best over-all performance on the basis of specific fuel consumption and propulsive thrust as a result of its ability to attain a high total-pressure recovery without prohibitive external drag. The one-cone (low-angle cowl) inlet had the smallest external drag and was comparable in performance with the two-cone inlet. At the low Reynolds number of the present tests, the application of roughness on the spike tip of both the two-cone and the isentropic inlets eliminated laminar-boundary-layer separation and effected a reduction in the external drags through reductions in mass-flow spillage.

For the one-cone inlet with varying degrees of supersonic mass-flow spillage, the experimental values of additive drag agreed quite well with theoretical predictions. At angle of attack, theory tended to underestimate the pitching-moment coefficient, the normal force coefficient, and the angle-of-attack drag rise, particularly at the higher angles.

INTRODUCTION

For application at a particular Mach number, the aim of good inlet design is the attainment of a high total-pressure recovery and a low external drag. Often it is found that there is a conflict between these

1-23

objectives and one can be achieved only at the expense of the other. Consequently, a compromise between the internal and external flow geometries must be made. Currently, only limited data are available on diffuser performance at Mach numbers greater than 3.0. Therefore, in order to obtain further insight into the criteria involved in the design of high Mach number diffusers, the NACA has undertaken an experimental research program that includes the investigation of the various conventional annular nose inlets at a Mach number of 3.85.

The initial phase of this research, which is primarily concerned with the diffuser characteristics of pressure recovery and mass flow, is reported in reference 1. The second phase of the research, covered in the present report, is concerned chiefly with the drag aspect of high Mach number inlets. Accordingly, the experimental investigation was directed toward (1) the determination of the aerodynamic forces and moments acting on the various inlet configurations over a wide range of angles of attack, (2) the evaluation and component breakdown of the external drags at zero angle of attack, and (3) the determination of additive drag coefficient as a function of supercritical flow spillage behind a conical shock.

The experimental configurations (the same as those used in ref. 1) were axially symmetric annular nose inlets employing single-shock- and multishock-generating centerbodies, or, more specifically, one-cone, two-cone, and isentropic inlets. Pressure and three-component balance (normal-force, axial-force, and pitching-moment) measurements were obtained for each configuration operating over a range of angles of attack from 0° to 9° .

SYMBOLS

The following symbols are used throughout this report:

A	model flow area, sq ft
A_{\max}	maximum frontal area of model
A_1	maximum capture area defined by cowl-lip diameter, sq ft
C_A	axial-force coefficient, axial force/ $q_0 A_{\max}$
C_D	drag coefficient, $D/q_0 A_{\max}$
C_F	thrust coefficient, $F/q_0 A_{\max}$

$C_{F,p}$	propulsive thrust coefficient, $(F - D)/q_0 A_{\max}$
C_M	pitching-moment coefficient, $N\bar{X}/q_0 A_{\max}$
C_N	normal force coefficient, $N/q_0 A_{\max}$
D	drag, lb
F	thrust, lb
f/a	fuel-air ratio
L	over-all length of model (from spike tip to base), ft
M	Mach number
m_0	mass-flow rate through free-stream tube area equal to A_1 , slugs/sec
m_3	mass-flow rate through engine, slugs/sec
N	normal force, lb
P	total pressure, lb/sq ft
p	static pressure, lb/sq ft
q	dynamic pressure, $\gamma p M^2/2$, lb/sq ft
\bar{X}	center of pressure location (measured from base), ft
α	angle of attack, deg
γ	ratio of specific heats for air
η_{ke}	kinetic energy efficiency defined as ratio of kinetic energy available after diffusion to kinetic energy in free stream,

$$1 - \frac{2}{(\gamma - 1)M^2} \left[\left(\frac{P_0}{P_3} \right)^{\frac{\gamma-1}{\gamma}} - 1 \right]$$

θ_2	cowl-position parameter, angle between axis and line from spike tip to cowl lip, deg
------------	---

Subscripts:

a	additive
c	cowl pressure
e	external
f	friction
0	free stream
3	diffuser exit
4	model exit

3028

APPARATUS AND PROCEDURE

The experimental investigation was conducted in the NACA Lewis 2- by 2-foot supersonic wind tunnel, which was operated at a Mach number of 3.85 and at a simulated pressure altitude of approximately 108,000 feet. The tunnel air was maintained at a stagnation temperature of $200^{\circ} \pm 5^{\circ}$ F and at a dew-point temperature of $-10^{\circ} \pm 10^{\circ}$ F. Based on the maximum diameter of the cowl (5 in.), the Reynolds number was approximately 429,000.

As illustrated in figure 1, the experimental model, which utilized an adjustable exit plug to vary the inlet back pressure, was basically the same as the model of reference 1, with the exception of the three-component force-measuring system. Details of the balance link are revealed in the insert drawing on figure 1(a). Mounted on the flexural members of the link are electric resistance-wire strain gages, which, connected in bridge circuits, provide the indications of axial and normal forces and pitching moment. Some interaction of the force components was encountered with this balance system, but the effects were accounted for in the calibration and eliminated from the data. Tare forces acting on the base of the model and within the sting balance chamber were determined and subtracted out of the axial-force data.

Specifications of the various inlet configurations are presented in coordinate form in table I and in the sketches of figure 1(b). The one-cone inlet consisted of a 60° -included-angle cone positioned so that, theoretically, the cowl lip would just intercept the tip shock emanating from the centerbody (design $\theta_1 = 44.9^{\circ}$). A gradual rate of turning of the flow back toward the axial direction with no internal

contraction was effected by the cowl, which was initially alined in the local stream direction. In an attempt to achieve a near-minimum cowl-pressure drag, a second single-oblique-shock configuration, designated the one-cone (low-angle cowl) inlet, was made with a sharp turn at the cone shoulder and a cylindrical internal contour on the cowl. As described in reference 1, the application of local suction immediately downstream of the sharp turn was required for attached shocks to exist at the cowl lip. This suction was accomplished by means of a double row of 1/8-inch-diameter bleed holes on the centerbody, the inside of which was vented to ambient tunnel pressure by means of hollow centerbody support struts.

The two-cone inlet was designed with two conical surfaces (40° and 70° included angles) that would, theoretically, locate the resulting shocks at the cowl lip. Additional flow compression was attempted by applying the maximum permissible internal contraction (ref. 2) based on an estimated average entrance Mach number.

Of the four inlet configurations being considered, theoretically the greatest amount of supersonic compression would be obtained with the isentropic inlet, which utilizes a continuously curved centerbody to produce the desired turning of the flow. In the theoretical characteristics solution, the Mach waves were designed to focus at the cowl lip, the internal contour of which was initially arranged in the local flow direction. The compression was to be carried down to a final Mach number of approximately 1.5 with no internal contraction.

In order to circumvent the difficulty of laminar-boundary-layer separation encountered on both the two-cone and the isentropic inlets, an attempt was made to promote an artificially induced transition from a laminar to a turbulent boundary layer. This transition was to be accomplished by the application of tip roughness in the form of a 1/2-inch band of (number 60) carborundum grit.

Pressure instrumentation consisted of eight wall and rake static orifices plus a 24-tube pitot rake at the end of the subsonic diffuser (see fig. 1(f) of ref. 1). Static taps were located on the top, side, and bottom of the base annulus. A static tap was also used to measure the pressure inside the sting balance chamber, and three rows of external wall static taps were installed along the cowl on the top, side, and bottom of each inlet configuration. In order to determine the boundary-layer profiles along the external shell in the vicinity of the base, a traversing total-pressure probe mounted to the tunnel wall was used to survey the flow field. A static orifice was also located on the external shell in the survey plane.

The total pressure at the diffuser exit was determined through an area-weighting of the pitot-rake measurements, while the mass flow

passing through the model was calculated with the assumption of one-dimensional flow from the average static pressure at the rake and the sonic discharge area. An integration of the cowl static-pressure distributions yielded values of cowl-pressure drag; friction drag was obtained from the integrations of boundary-layer-profile data, with a constant static pressure and total temperature assumed throughout the boundary layer. In the calculations of internal thrust, the evaluation of the exit momentum term was based on the pressure measurements at the exit rake.

Cowl-pressure drags were determined only at zero angle of attack. Otherwise, complete force and pressure data were recorded at angles of attack of 0° , 3° , 6° , and 9° over a wide range of exit plug positions. A twin-mirror schlieren system provided a means of visual observation of the inlet flow patterns under all test conditions.

RESULTS AND DISCUSSION

Before presenting the results of this investigation it should be emphasized that these experiments dealt with the evaluation of specific inlet geometries that were believed to be representative of the better designs within each category - that is, one-cone, two-cone, and isentropic inlets. However, a certain amount of arbitrariness was involved in the designs, for example, in the rate of turning the flow back toward the axial direction, in the rate of subsonic diffusion, or in the manner of coping with shock - boundary-layer interactions. Optimization of the respective designs, therefore, may influence the relative over-all performances of these inlets. Further research in this direction will be necessary for final evaluation.

Internal-Flow Performance

Although the diffuser performance (internal-flow) characteristics of the several inlet configurations were extensively detailed in reference 1, they are again included herein (fig. 2) for completeness and because there were minor differences between the values obtained during the force tests and those previously presented. Schlieren photographs of the inlet shock structure during supercritical operation are also included in the figures for angles of attack of 0° , 3° , 6° , and 9° . In figure 2(g), the data are summarized by cross-plotting the optimum points of each configuration in order to provide a relative comparison of the various inlets. At zero angle of attack the isentropic inlet had the highest total-pressure recovery (0.57), corresponding to a kinetic-energy efficiency η_{ke} of 0.94, but fell off quite sharply with increasing angle of attack until at 7.5° the flow separated completely

off the lee side of the spike. This separation occurred with an attendant hysteresis wherein the angle of attack had to be reduced to approximately 6.3° before an attached flow was reestablished. For angles of attack greater than approximately 7° , the total-pressure recovery of the two-cone inlet exceeded that of the isentropic. On both the two-cone and the isentropic spikes the application of tip roughness appeared to eliminate the "bridging" (or separation) of the laminar boundary layer due to the adverse pressure gradient and resulted in improved inlet pressure recovery and mass-flow ratio.

At zero angle of attack the supercritical mass-flow ratio for the one-cone inlet was varied from 1.00 to 0.73 by controlling the amount of flow spillage behind the conical shock through changes in the value of the cowl-position parameter θ_1 from 45.5° to 42.5° . These changes were accomplished by inserting spacer rings behind the cowl in order to vary the spike-tip projection. The resulting diffuser performance characteristics are presented in figure 3. With decreasing supercritical mass-flow ratio, or equivalently increasing spillage, the maximum total-pressure recovery decreased nearly linearly. Even with the conical shock passing well ahead of the cowl lip ($\theta_1 = 42.5^\circ$), there was no indication of any degree of subcritical flow stability as might have been expected on the basis of the slipline criterion of reference 3. The aerodynamic instability or buzz could quite feasibly have been triggered by a local flow separation occurring internally on the centerbody (as illustrated in ref. 4), or in the vicinity of the terminal shock (as predicted by the criterion of ref. 5), or both.

Force Measurements at Zero Angle of Attack

The force data for the one-cone inlet at zero angle of attack with several values of the cowl-position parameter θ_1 are presented in figure 4, where the variations of internal thrust, propulsive thrust, and external drag coefficients with outlet-inlet area ratio are plotted. On each set of curves are included the experimentally determined values of cowl-pressure drag coefficient $C_{D,c}$, the friction drag coefficient $C_{D,f}$, and the theoretical additive drag coefficient $C_{D,a}$, as given in reference 6. Based on the experimental profiles, the boundary layer along the external shell of the model was turbulent with a corresponding skin-friction coefficient of approximately 0.002. The heavy line represents a summation of the preceding components of the total external drag. The data points for external drag are experimental values obtained by subtracting the propulsive (or net) thrust coefficients, as determined by actual balance measurements, from the internal thrust coefficients, as calculated from the change in total momentum across the engine. As illustrated by figure 4, a very close agreement was obtained between the two methods of arriving at values of the external drag, that

is, by component summations and by actual force measurements used in conjunction with internal pressure measurements. The external drag coefficient increased from 0.17 to 0.28 as θ_2 was changed from 45.5° to 42.5° or, correspondingly, as the capture mass flow decreased from 1.00 to 0.73 (fig. 3). This drag increase essentially represented the additive drag contribution resulting from flow spillage behind the conical shock. A comparison of the experimental and theoretical additive drag coefficients is presented in figure 5 as a function of supercritical mass-flow ratio. These experimental values were determined by subtracting the measured cowl-pressure and friction drag components from the internal thrust. As shown, the data agreed rather well with the predictions of reference 6.

In figure 6 the force data are presented for the one-cone (low-angle cowl), the two-cone, and the isentropic inlets at zero angle of attack. Except for the two-cone with tip roughness and the one-cone (low-angle cowl) inlets, there was no theory readily available for the estimation of additive drags; and, therefore, the horizontal lines of $C_{D,e}$ represent more or less mean values drawn through the balance data. The theoretical value of $C_{D,a}$ listed for the one-cone (low-angle cowl) inlet is somewhat approximate, in that the 1 percent of the maximum capture mass flow m_0 involved in the suction process (ref. 1) was considered to have undergone a complete loss of momentum. The greatest scatter in the data occurred with the isentropic inlets near the critical condition; and, in these cases, the higher, more supercritical values were favored, because it was felt that the calculation of internal thrust might have been least accurate when the pressure measurements (which establish M_3) were made with an extremely low dynamic pressure q_3 .

A tabulation of the foregoing data (table II) provides a direct comparison of the performance of the various inlets at zero angle of attack. The most significant result was the moderately low value of external drag ($C_{D,e} = 0.16$) achieved with the isentropic inlet with tip roughness. An examination of the components of this drag showed a relatively low cowl-pressure drag (associated with the fact that the design allowed for a small projected area on the cowl) and only a slightly greater amount of additive drag than that for the one-cone inlet at a comparable mass-flow ratio. This additive drag coefficient for the isentropic inlet with tip roughness amounted to much less than the value for complete momentum loss, assumed as a maximum in reference 1, and was also somewhat less than the minimum calculated from the theoretical characteristics solution that had the Mach waves coalescing at the cowl lip. The total external drag coefficients for the isentropic with tip roughness, the two-cone with tip roughness, and the one-cone inlets were approximately the same. As a consequence of a negligibly small cowl-pressure drag

~~CONFIDENTIAL~~

($C_{D,c} = 0.009$), the one-cone (low-angle cowl) inlet exhibited the lowest external drag ($C_{D,e} = 0.09$). Again, it is quite evident that for the one-cone inlet the increase in external drag coefficient with decreasing values of θ_1 was due almost entirely to the increase in additive drag.

Over-All Performance Comparison at Zero Angle of Attack

In order to evaluate the over-all performance of the various inlet configurations and to establish a basis of relative merit in which the combined factors of total-pressure recovery, mass-flow ratio, and external drag would be taken into account, the experimental values for each inlet (table II) were incorporated into the calculations for application to a hypothetical ram-jet engine. The assumed operating conditions for this engine were as follows: flight Mach number of 3.85 at 80,000 feet altitude, critical inlet performance at zero angle of attack, 90-percent combustion efficiency, and complete exit-nozzle expansion. The 80,000-foot altitude used in this comparison differs from the actual simulated pressure altitude of the present experiments; however, it was selected because it conforms to a more practical flight condition, as indicated in recent ram-jet analyses. As a result, then, the assumption is made that the Reynolds number effect would be negligibly small, at least with respect to the relative performances of the various inlets. The results of these calculations are presented in figure 7 for a range of fuel-air ratio f/a . On the basis of specific fuel consumption, the one-cone (low-angle cowl) inlet was comparable with the two-cone inlet with tip roughness, and the specific fuel consumption of the isentropic inlet with tip roughness was 8 percent lower than that obtained with either of the preceding inlets over the entire fuel-air-ratio range. At a fuel-air ratio of 0.03, the isentropic inlet with tip roughness exhibited a specific fuel consumption approximately 20 percent lower than that of the one-cone inlet. At $f/a = 0.03$, the propulsive thrust of the one-cone (low-angle cowl) inlet was 15 percent, of the two-cone inlet with tip roughness 28 percent, and of the isentropic inlet with tip roughness 55 percent greater than that of the one-cone inlet. The values of propulsive thrust coefficient $C_{F,p}$ on this figure were based on A_{max} for the engine, which was at the exit. To permit conversion to any other reference area, the ratio of A_{max}/A_0 was also included.

Of the configurations studied, then, the isentropic inlet with tip roughness has the best performance at zero angle of attack in terms of specific fuel consumption and propulsive thrust. These results are due to the attainment of a high total-pressure recovery without prohibitive external drag.

~~CONFIDENTIAL~~

Angle-of-Attack Force Measurements

Force data obtained for each of the respective inlet configurations at angle of attack are given in figure 8, where the variations of axial-force, normal force, and pitching-moment coefficients are presented as a function of outlet-inlet area ratio for angles of attack of 3° , 6° , and 9° . In general, the pitching-moment coefficient C_M was independent of diffuser back pressure during supercritical operation and increased with increasing angle of attack. There was considerable variation of the normal force coefficient C_N with supercritical values of A_4/A_1 . This may be attributed in part to some distortion of the exit flow conditions due to local separation of the internal flow, which was illustrated by the velocity profiles presented in reference 1 for angles of attack of 3° and above and which might have caused the mean exit flow direction to be other than axial. Generally, however, the absolute level of C_N increased with increasing angle of attack. Also included in the figures are the values of axial-force (or thrust-minus-drag) coefficients. The magnitude of axial-force coefficient C_A is not overly significant in itself, since it simulates the force corresponding to burning and choking in a constant-area duct with a required heat release beyond the range of present-day hydrocarbon fuels. For critical inlet operation, the axial force decreased with increased angle of attack, as would be expected.

A comparison was made between the angle-of-attack force data and the theory of reference 7, modified for an open-nose body, by taking into account the internal-flow contributions. Pitching-moment coefficients (fig. 9) and normal force coefficients during critical inlet operation (fig. 10) tended to fall above the theoretical values, particularly at the higher angles of attack.

Attempts to extract the external drag coefficients at angle of attack from the data were not very successful. The previously mentioned internal-flow separation at angle of attack prevented a consistent calculation of internal thrust based on the pressure data. Since the method of data reduction involved a subtraction of the propulsive thrust (or thrust-minus-drag) term from the internal thrust, a large amount of scatter was incurred. The resulting data points, along with corresponding bands of experimental scatter, are presented in figure 11. Also included is the theoretical drag rise due to angle of attack ($C_{D,e} - C_{D,e,\alpha=0^\circ}$). By way of comparison, a composite curve drawn through the experimental data indicated the drag rise due to angle of attack to be much more rapid than that predicted by theory. Based on these crude data, a specific-fuel-consumption comparison of the various inlets appeared to indicate that the isentropic inlet would be superior up to approximately 6° angle of attack.

The experimental data, locating the center of pressure at angle of attack, also exhibited considerable scatter but appeared to fall fairly well in the following bracket for all inlet configurations:

$$0.45 > \frac{\bar{X}}{L} > 0.60$$

where \bar{X} is the distance of the center of pressure measured from the base and L is the over-all length of the model (from spike tip to base).

SUMMARY OF RESULTS

An experimental investigation to evaluate the over-all force and pressure characteristics of four annular nose inlets, designated the one-cone, the one-cone (low-angle cowl), the two-cone, and the isentropic inlets, yielded the following results at a Mach number of 3.85:

1. At zero angle of attack, the isentropic inlet with tip roughness showed the most promise of the inlet configurations studied, as a result of its ability to attain a high total-pressure recovery (0.57) without a prohibitive external drag ($C_D = 0.16$ based on the maximum cowl area). The performance of a hypothetical ram-jet engine utilizing this inlet, based on specific fuel consumption and propulsive thrust, exceeded that obtained with any of the other configurations up to an angle of attack of approximately 6° .
2. At zero angle of attack, the low external drag obtained with the one-cone (low-angle cowl) inlet ($C_{D,e} = 0.09$) made it comparable with the two-cone inlet with tip roughness on the basis of specific fuel consumption and propulsive thrust.
3. At the low Reynolds number of these experiments, the application of tip roughness on both the two-cone and the isentropic inlets resulted in slightly higher total-pressure recoveries and lower external drags through reduced mass-flow spillage.
4. For the one-cone inlet with various degrees of supersonic mass-flow spillage, the experimental values of additive drag were in good agreement with theoretical predictions. In addition, the external drag coefficients obtained by a summation of components agreed quite well with those derived from the balance measurements.
5. At angle of attack, theory tended to underestimate the pitching-moment coefficient, the normal force coefficient, and the angle-of-attack drag rise, particularly at the higher angles.

Lewis Flight Propulsion Laboratory
National Advisory Committee for Aeronautics
Cleveland, Ohio, October 7, 1953

~~CONFIDENTIAL~~

3028

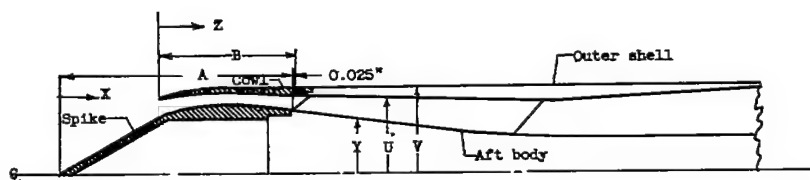
CZ-2 back

REFERENCES

1. Connors, James F., and Woollett, Richard R.: Performance Characteristics of Several Types of Axially Symmetric Nose Inlets at Mach Number 3.85. NACA RM E52I15, 1952.
2. Kantrowitz, Arthur, and Donaldson, Coleman duP.: Preliminary Investigation of Supersonic Diffusers. NACA WR L-713, 1945. (Supersedes NACA ACR L5D20.)
3. Ferri, Antonio, and Nucci, Louis M.: The Origin of Aerodynamic Instability of Supersonic Inlets at Subcritical Conditions. NACA RM L50K30, 1951.
4. Connors, James F., and Woollett, Richard R.: Some Observations of Flow at the Throat of a Two-Dimensional Diffuser at a Mach Number of 3.85. NACA RM E52I04, 1952.
5. Donaldson, Coleman duP., and Lange, Roy H.: Study of the Pressure Rise Across Shock Waves Required to Separate Laminar and Turbulent Boundary Layers. NACA TN 2770, 1952. (Supersedes NACA RM L52C21.)
6. Sibulkin, Merwin: Theoretical and Experimental Investigation of Additive Drag. NACA RM E51B13, 1951.
7. Allen, H. Julian: Estimation of the Forces and Moments Acting on Inclined Bodies of Revolution of High Fineness Ratio. NACA RM A9I26, 1949.

3028

TABLE I - INLET DIMENSIONS



Aft body		Outer shell		
X	Y	Z	U	V
A	1.82	B	2.30	2.50
↓	Straight	↓	Straight	↓
A + 4.50	taper	B + 7.186	taper	Cylin-
↓	1.22	↓	2.06	dricial
A + 9.13	Straight	B + 7.625	1-in.-	↓
↓	taper	↓	rad. arc	↓
A + 14.25	Straight	B + 12.75	2.065	↓
	cylinder	↓	2.375	↓
	2.00			2.50

A length of spike from tip to point of attachment to aft body, in.

B length of cowl from lip to point of attachment to outer shell, in.

One cone				
Spike (A, 6.370)		Cowl (B, 5.750)		
X	Y	Z	U	V
0	0	0	2.132	2.132
↓	Straight	↓	2.186	2.211
3.000	taper	.100	2.223	2.262
3.100	1.731	.200	2.278	2.347
3.200	1.782	.300	2.318	2.411
3.400	1.824	.400	2.345	2.454
3.600	1.867	.500	2.363	2.483
3.800	1.906	.600	2.375	2.500
4.000	1.948	.700	2.373	Cylin-
4.200	1.988	.800	2.368	dricial
4.400	1.955	.900	2.360	↓
4.600	1.947	1.000	2.350	2.500
5.000	1.930	5.750	2.500	
5.500	1.898			
6.000	1.860			
6.370	1.820			

One cone (low-angle cowl)				
Spike (A, 7.10)		Cowl (B, 4.287)		
X	Y	Z	U	V
0	0	0	2.300	2.300
↓	Straight	↓	Cylin-	↓
3.292	taper	2.860	dricial	Straight
4.062	1.902	↓	2.300	taper
4.500	1.898	4.288	2.500	2.500
5.000	1.890			
5.500	1.880			
6.000	1.870			
6.300	1.862			
6.800	1.842			
7.100	1.820			

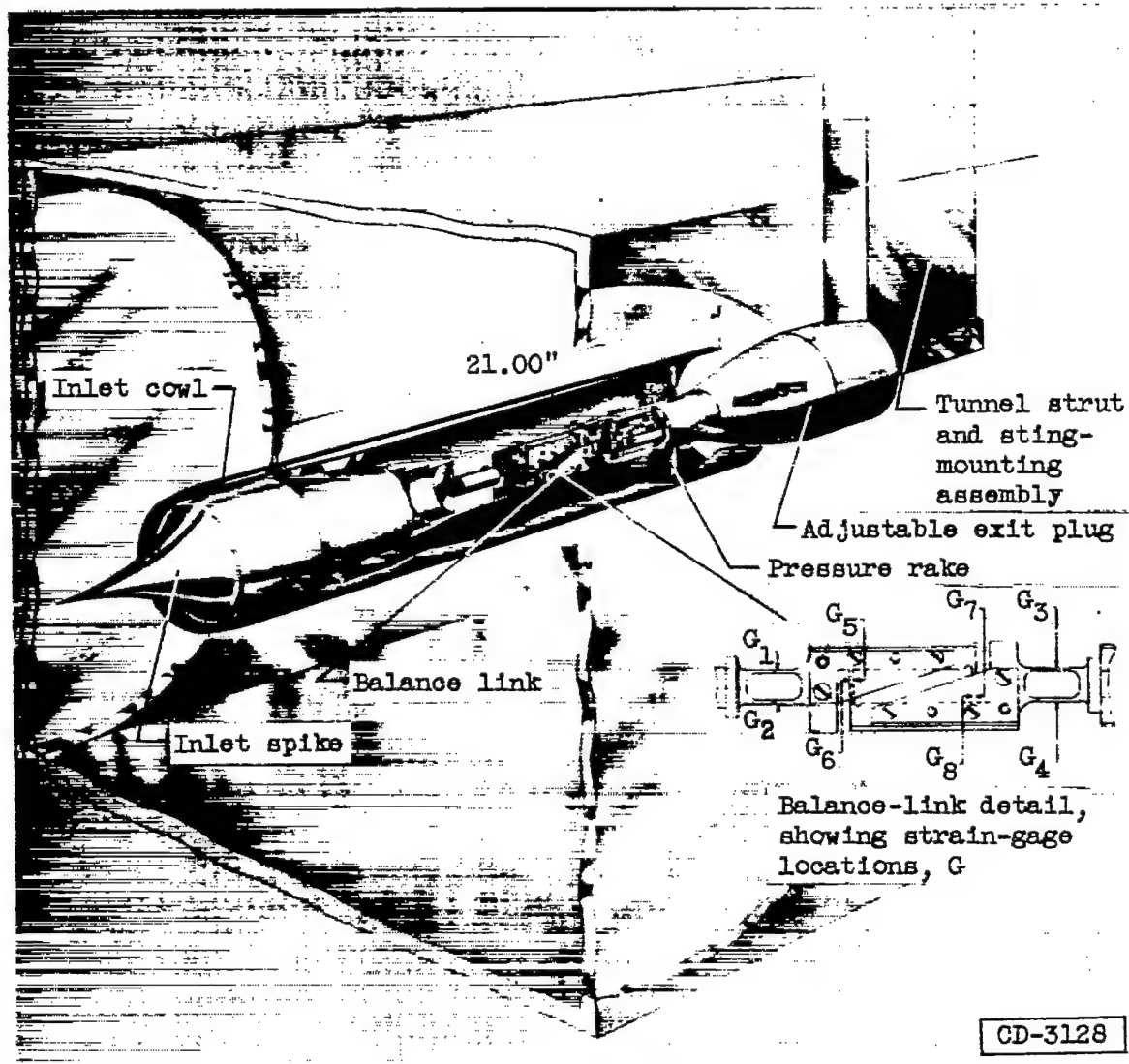
Two cone				
Spike (A, 9.852)		Cowl (B, 5.750)		
X	Y	Z	U	V
0	0	0	2.165	2.165
↓	Straight	↓	2.203	2.219
3.802	taper	.100	2.239	2.266
↓	1.384	.200	2.269	2.316
4.452	Straight	.300	2.295	2.358
↓	taper	.400	2.330	2.419
4.552	1.854	.500	2.352	2.459
4.652	1.902	.600	2.364	2.483
4.752	1.953	.700	2.372	2.497
4.852	1.993	.800	2.375	2.500
4.952	2.054	.900	2.375	Cylin-
5.152	2.095	1.000	2.375	dricial
5.352	2.119	5.750	2.375	↓
5.602	2.133	3.250	2.372	2.500
5.852	2.138	3.500	2.369	
6.102	2.136	3.750	2.365	
6.352	2.135	4.000	2.359	
6.652	2.116	5.750	2.300	
7.352	2.085			
7.852	2.048			
8.352	1.997			
8.852	1.943			
9.352	1.883			
9.852	1.820			

Isentropic				
Spike (A, 14.741)		Cowl (B, 7.750)		
X	Y	Z	U	V
0	0	0	2.240	2.240
.500	.075	.025	2.262	2.272
1.000	.145	.060	2.277	2.291
1.500	.216	.100	2.299	2.323
2.000	.284	.200	2.328	2.370
2.500	.357	.300	2.346	2.404
3.000	.436	.400	2.358	2.432
3.500	.528	.600	2.370	2.469
4.000	.624	.800	2.376	2.492
4.500	.742	1.000	2.378	2.500
5.000	.876	↓	Cylin-	↓
5.500	1.031	5.300	dricial	Cylin-
6.000	1.210	5.500	2.378	dricial
6.500	1.433	5.750	2.376	↓
7.000	1.748	6.000	2.370	2.500
7.100	1.830	6.000	2.360	
7.200	1.922	↓	Straight	↓
7.300	2.025	7.750	taper	2.500
7.400	2.100		2.300	
7.500	2.137			
7.600	2.159			
7.700	2.170			
8.000	2.178			
8.230	2.180			
9.000	2.174			
9.188	2.170			
10.000	2.153			
11.000	2.113			
12.000	2.060			
13.000	1.994			
14.000	1.906			
14.741	1.820			

TABLE II. - SUMMARY OF PERFORMANCE PARAMETERS FOR VARIOUS INLET CONFIGURATIONS
AT MACH NUMBER 3.85 AND ZERO ANGLE OF ATTACK

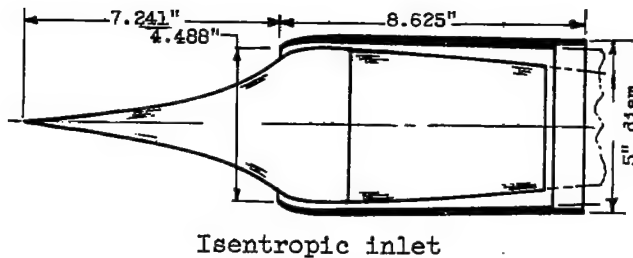
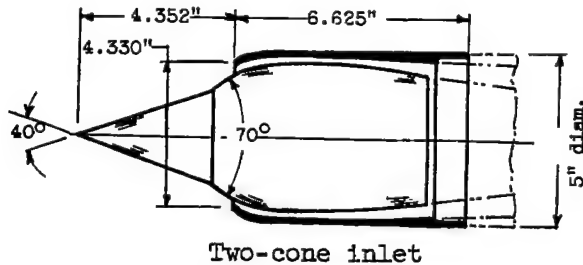
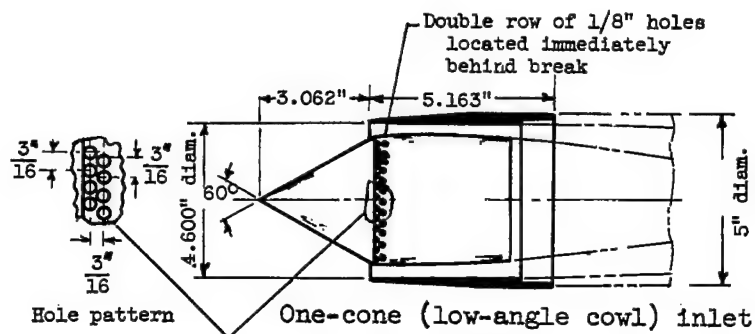
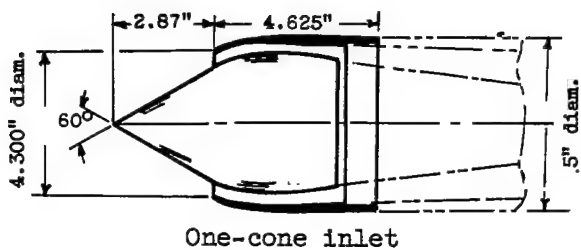
Annular nose-inlet configuration	Maximum total-pressure recovery, P_3/P_0	Supercritical mass-flow ratio, m_3/m_0	Cowl-pressure drag coefficient, $C_{D,c}$	Friction drag coefficient, $C_{D,f}$	Additive drag coefficient, $C_{D,a}$	Total external drag coefficient, $C_{D,e}$
One-cone: $\theta_1 = 45.5^\circ$	0.317	1.00	0.129	0.043	0	0.17
44.9°(design)	.311	.99	.127	.043	.003	.17
44.3°	.298	.934	.136	.043	.025	.20
43.7	.281	.865	.132	.043	.052	.23
43.1	.257	.800	.129	.043	.08	.25
42.5	.235	.728	.128	.043	.11	.28
One-cone (low-angle cowl)	0.30	0.925	0.009	0.044	0.037	0.09
Two-cone	0.40	0.875	0.114	0.047	^a 0.070	0.23
Two-cone with tip roughness	.44	.963	.114	.047	.008	.17
Isentropic	0.565	0.91	0.065	0.050	^a 0.075	0.19
Isentropic with tip roughness	.57	.93	.074	.050	^a .036	.16

^aDesignates experimental values for which there was no available theory to check against.



(a) Schematic drawing of 5-inch-diameter model installed in 2- by 2-foot supersonic tunnel.

Figure 1. - Experimental model.



(b) Inlet details.

Figure 1. - Concluded. Experimental model.

Supercritical flow patterns at various angles of attack

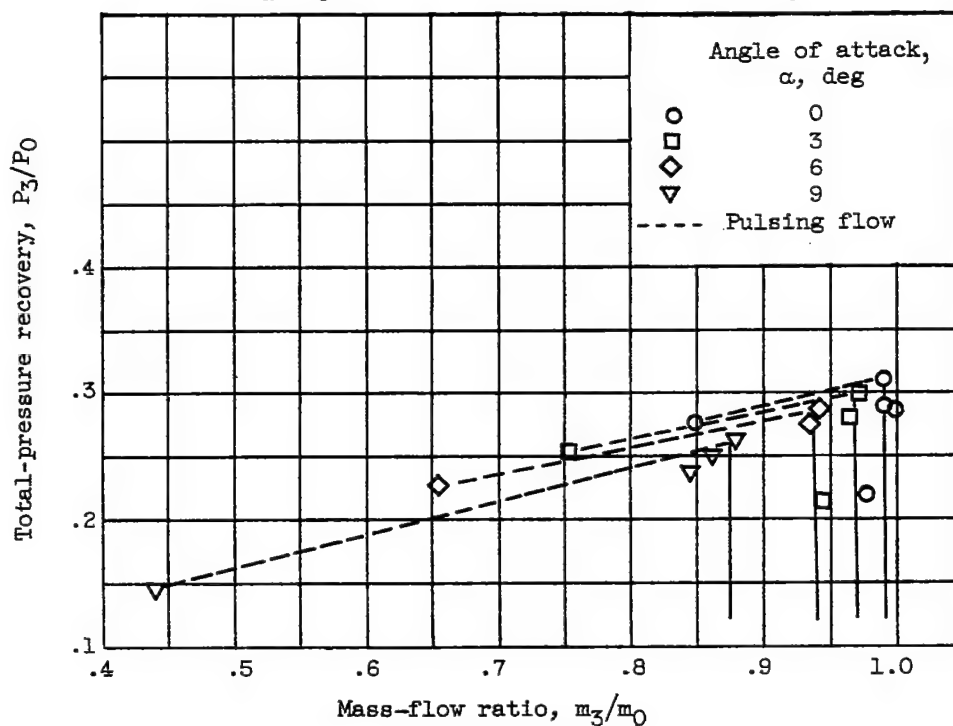
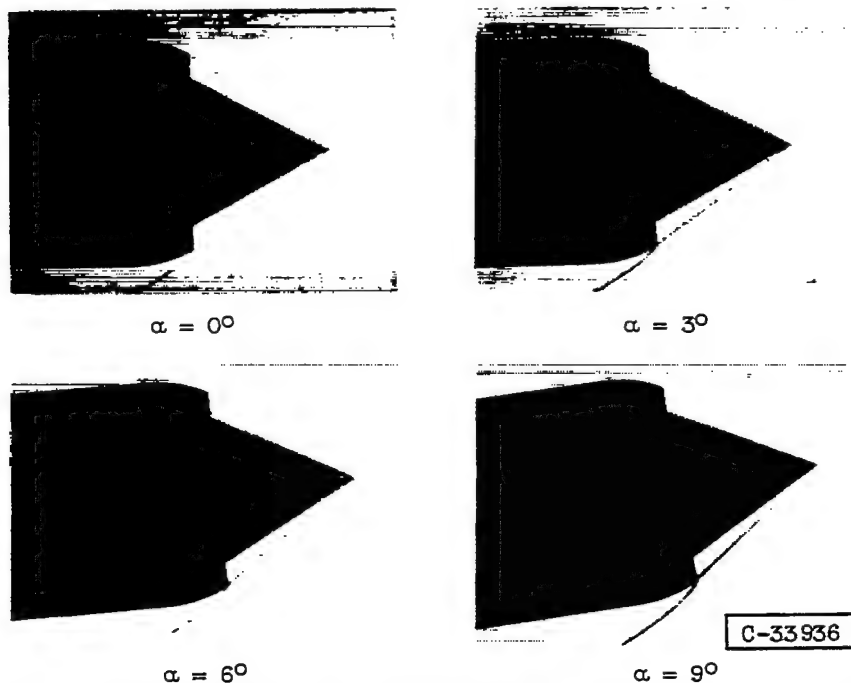
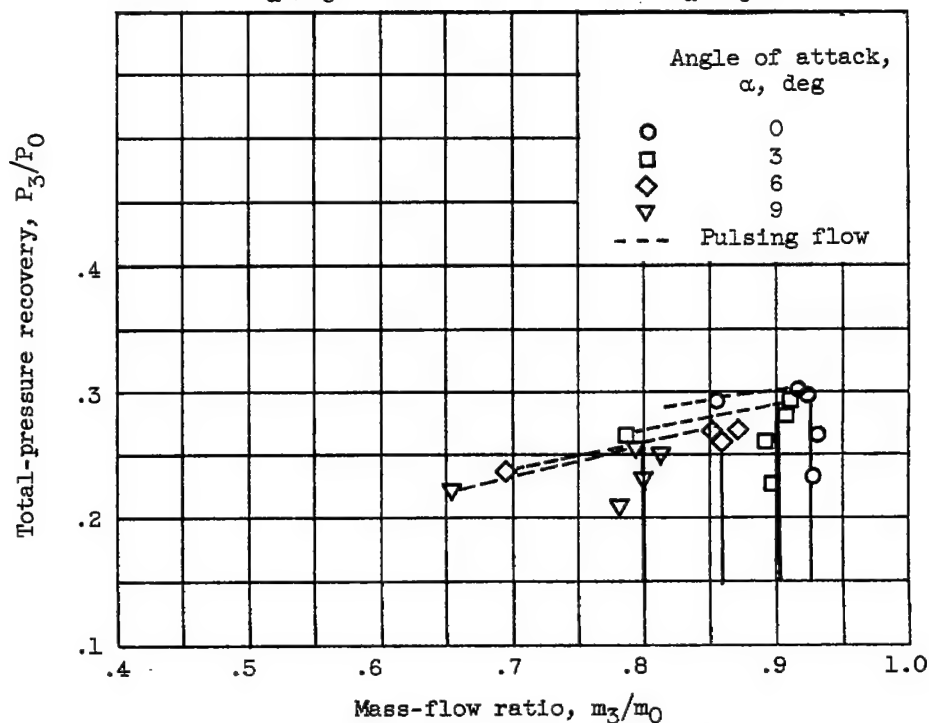
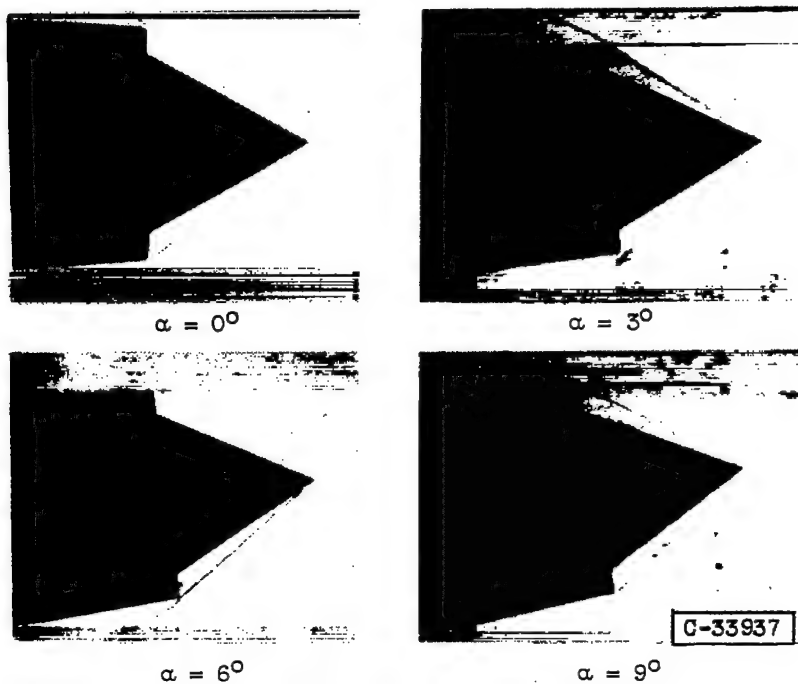


Figure 2. - Effect of angle of attack on inlet performance.

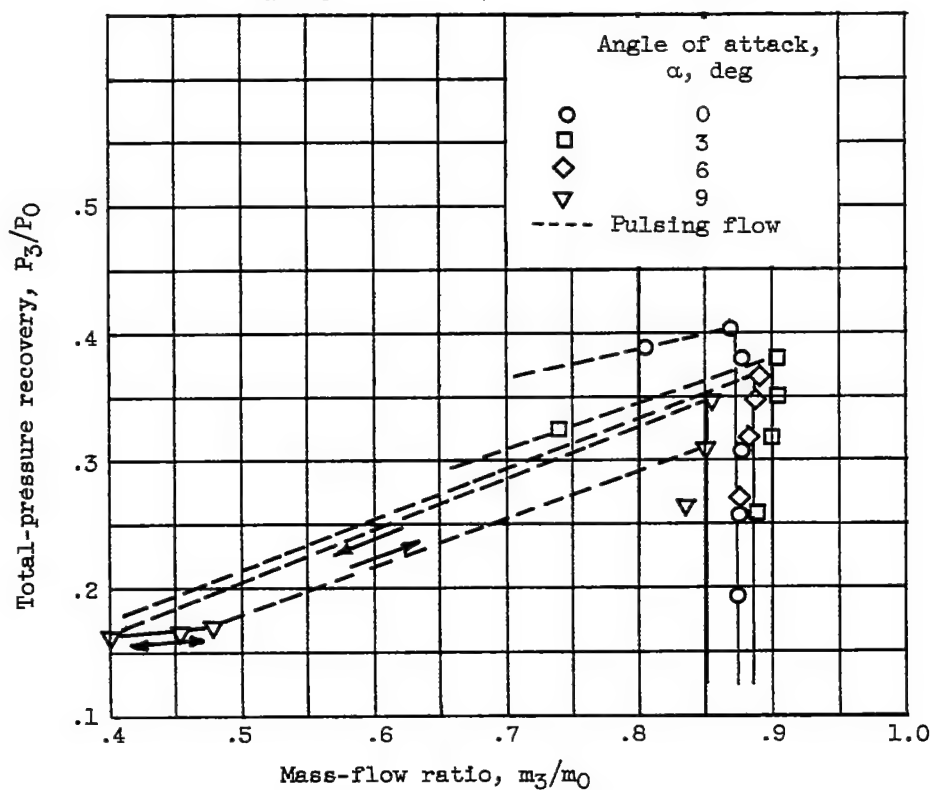
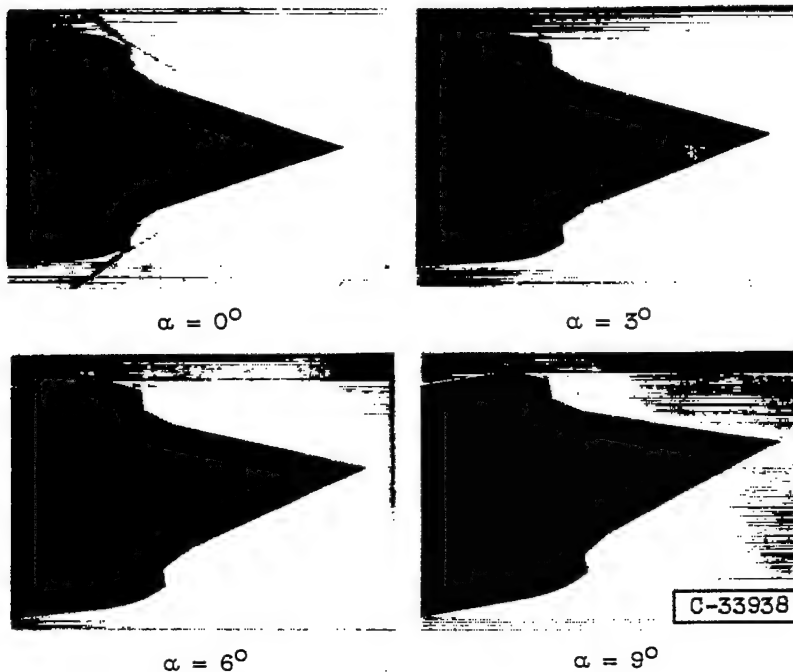
Supercritical flow patterns at various angles of attack



(b) One-cone (low-angle cowl) inlet.

Figure 2. Continued. Effect of angle of attack on inlet performance.

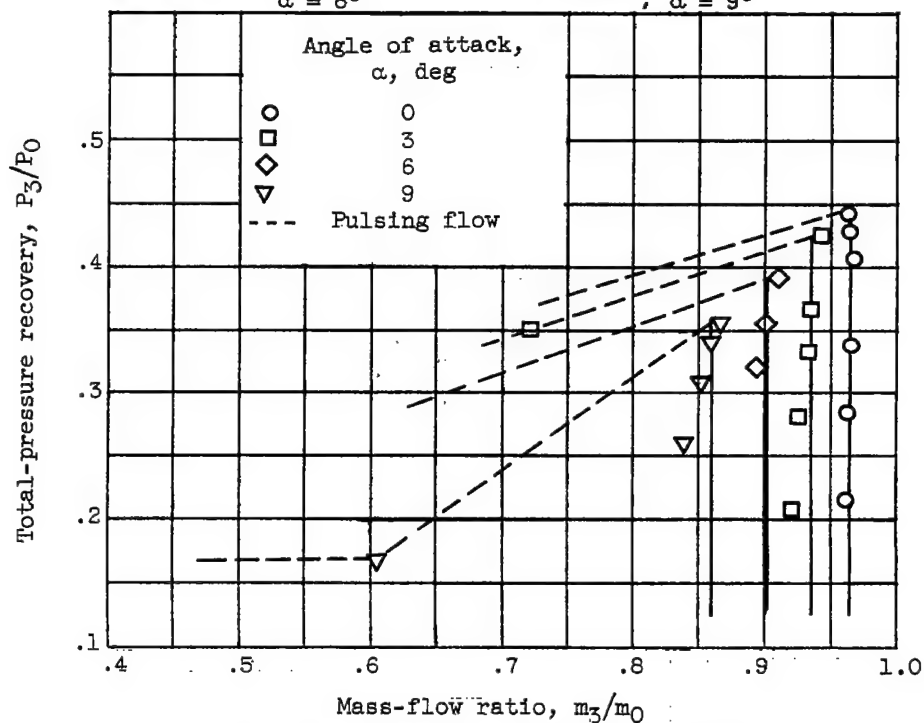
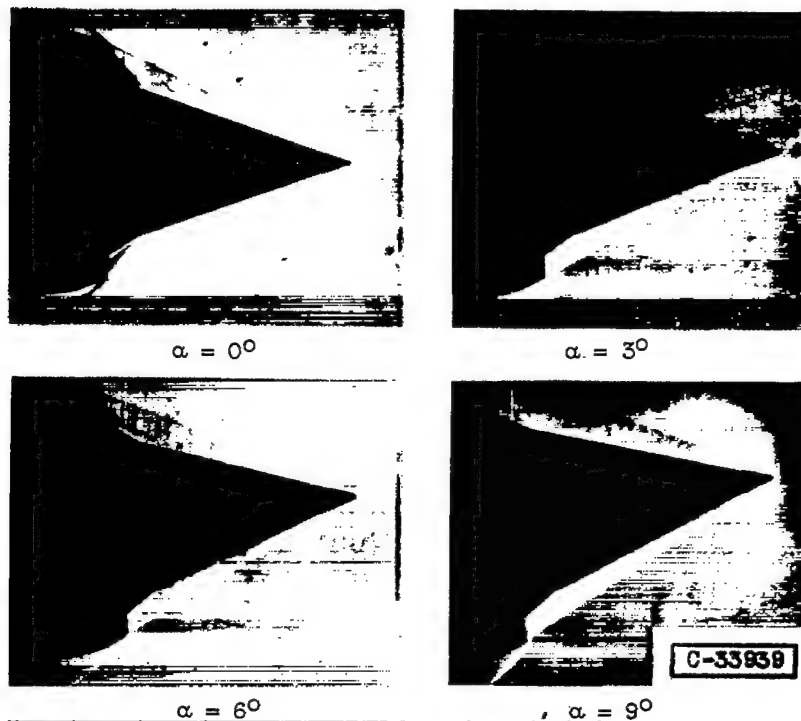
Supercritical flow patterns at various angles of attack



(c) Two-cone inlet.

Figure 2. - Continued. Effect of angle of attack on inlet performance.

Supercritical flow patterns at various angles of attack



(d) Two-cone inlet with tip roughness.

Figure 2. - Continued. Effect of angle of attack on inlet performance.

Supercritical flow patterns at various angles of attack

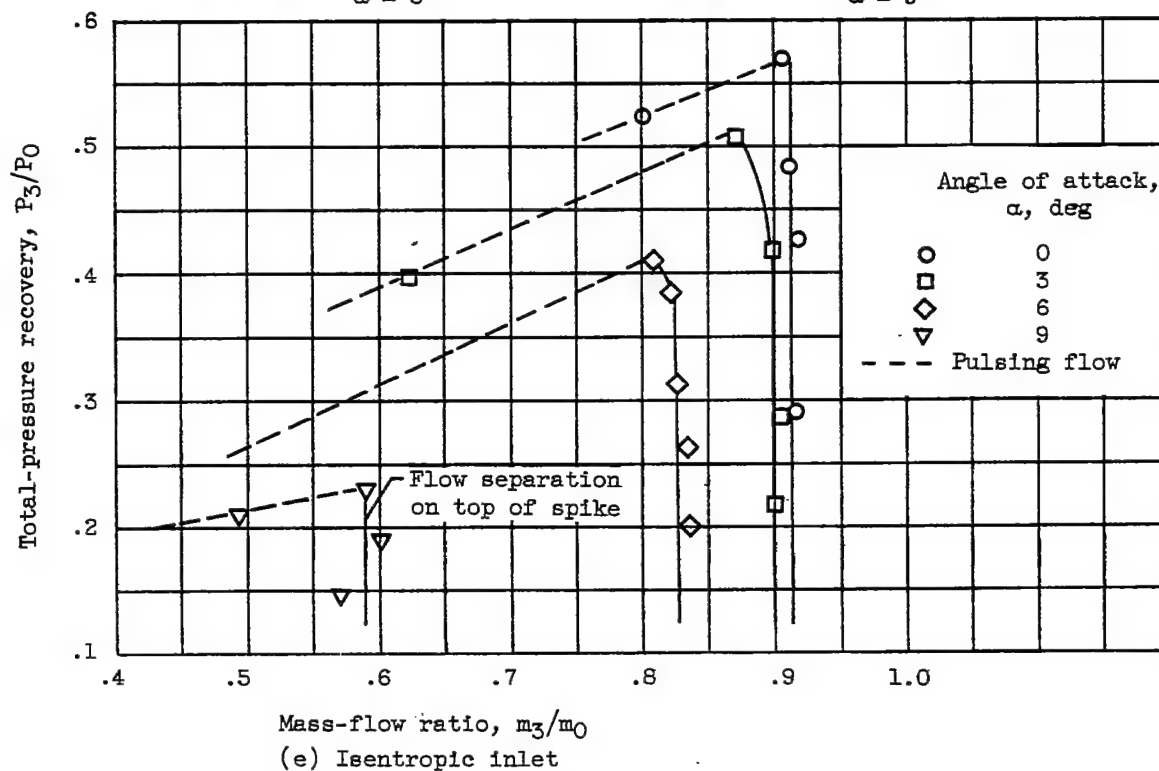
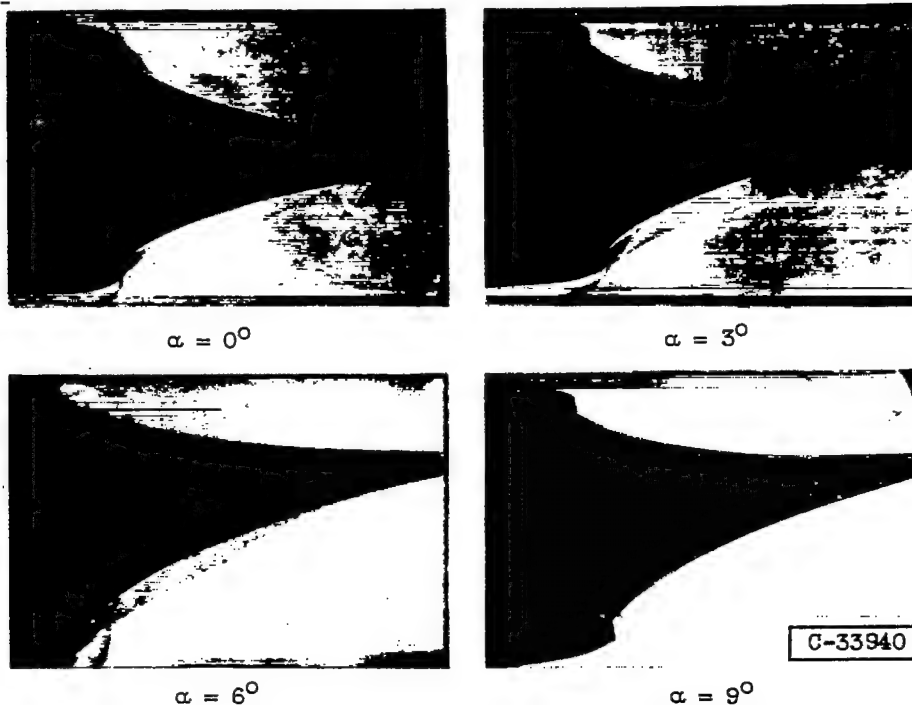
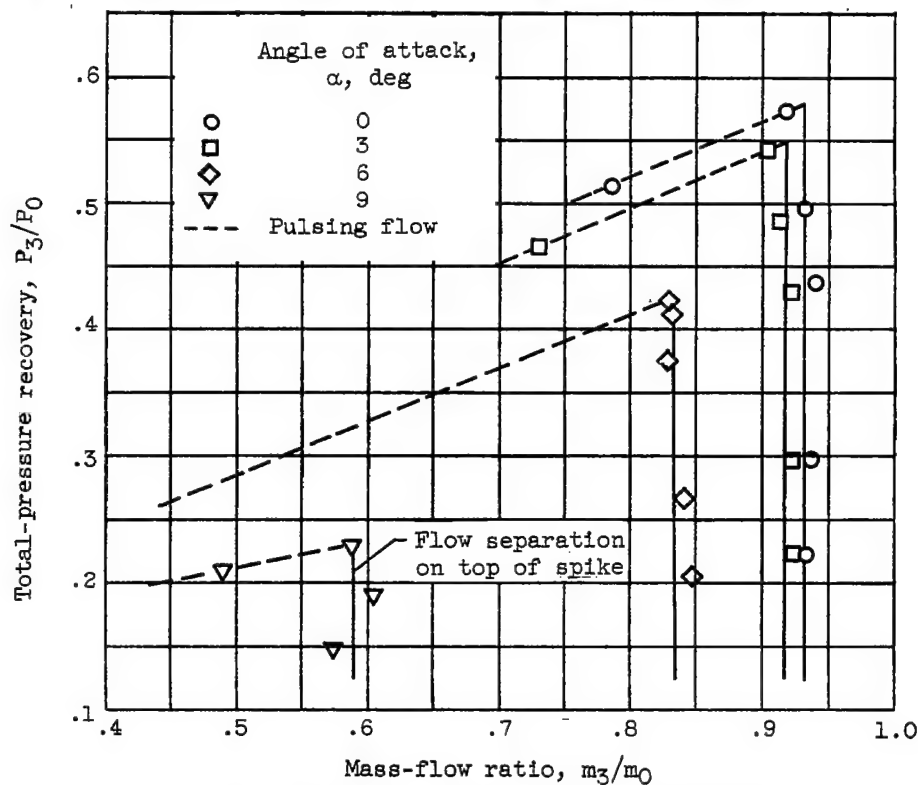
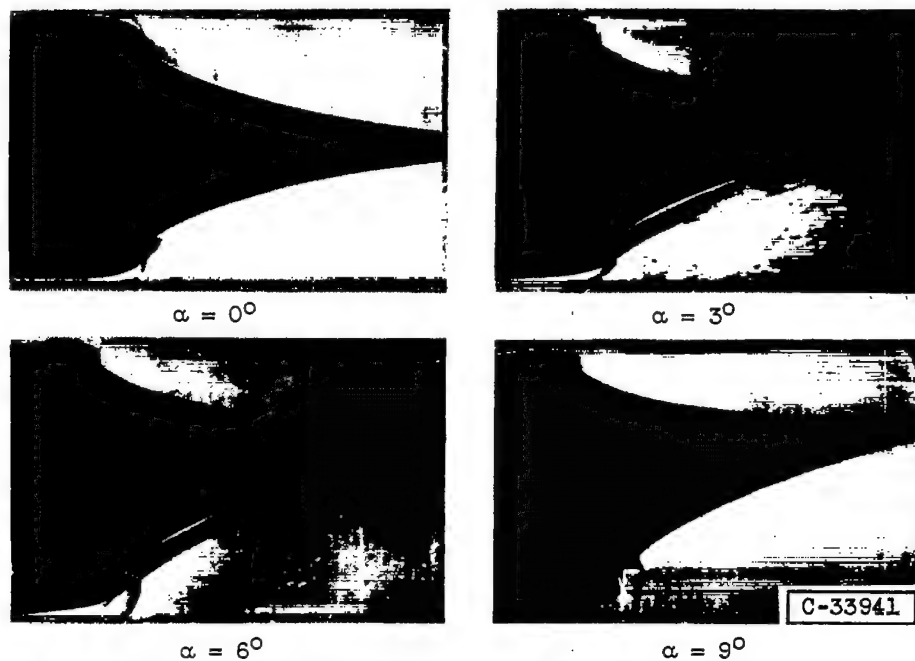


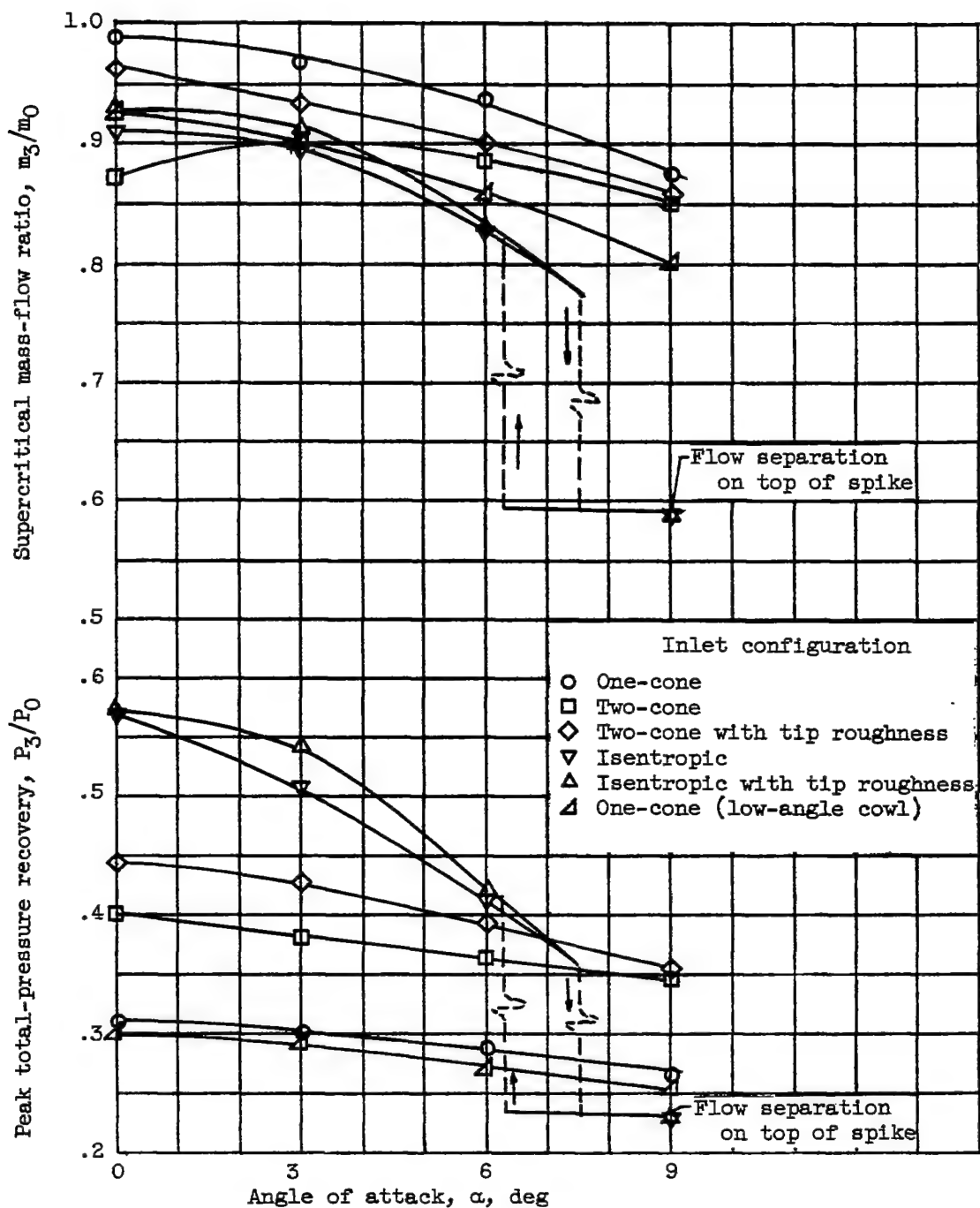
Figure 2. - Continued. Effect of angle of attack on inlet performance.

Supercritical flow patterns at various angles of attack



(f) Isentropic inlet with tip roughness.

Figure 2. Continued. Effect of angle of attack on inlet performance.



(g) Summary curves showing relative effects of angle of attack on performance of various inlet configurations.

Figure 2. - Concluded. Effect of angle of attack on inlet performance.

Supercritical flow patterns for several values of position parameter

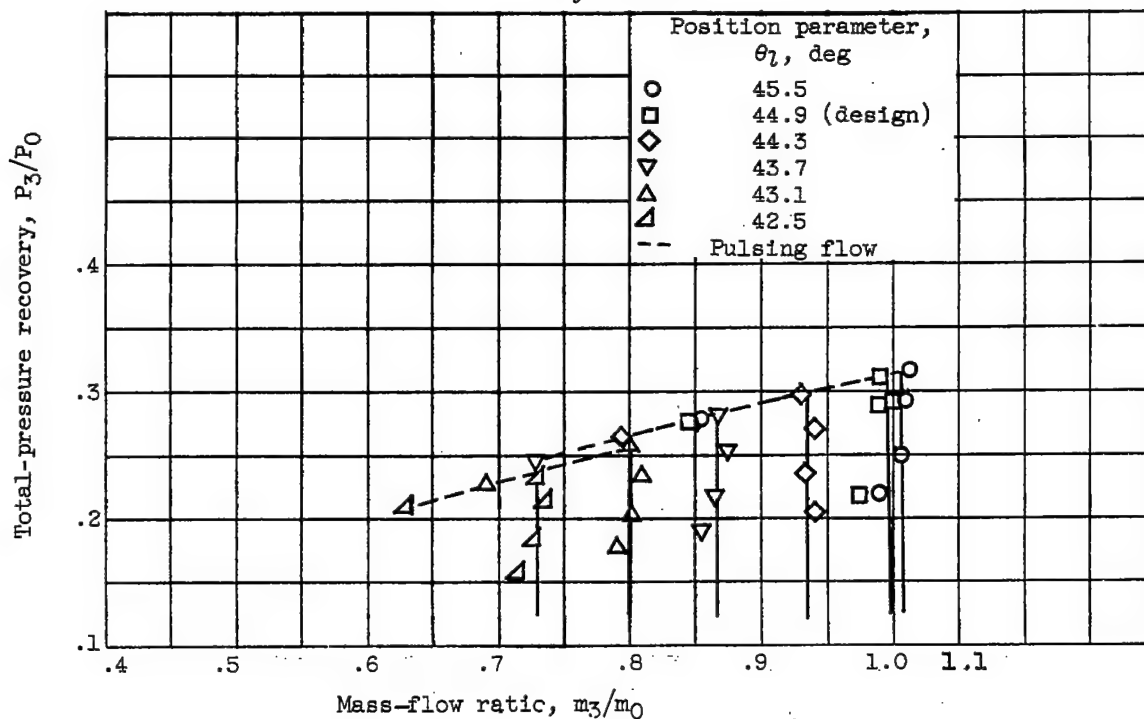
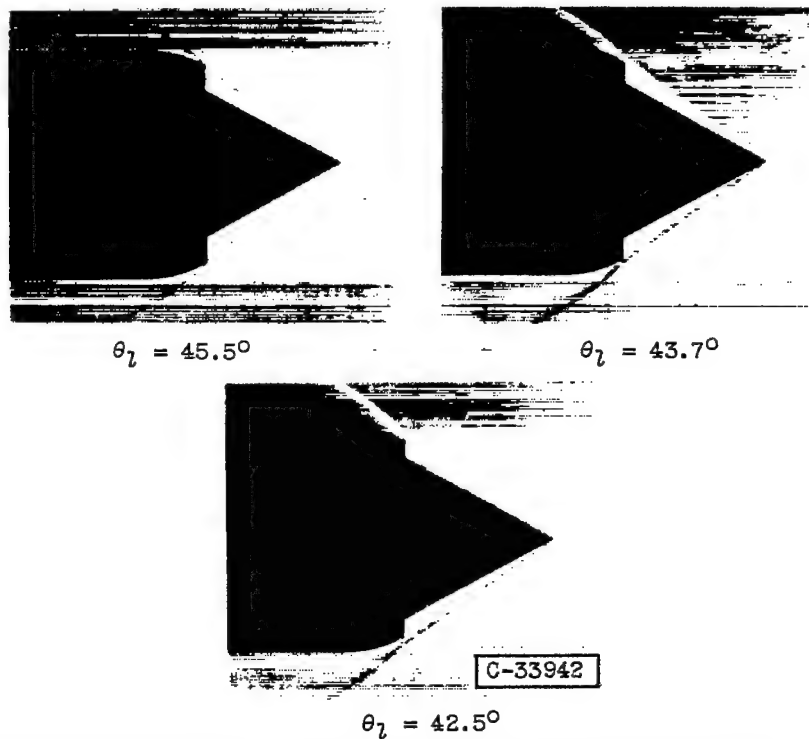


Figure 3. - Effect of position parameter on performance of one-cone inlet at zero angle of attack.

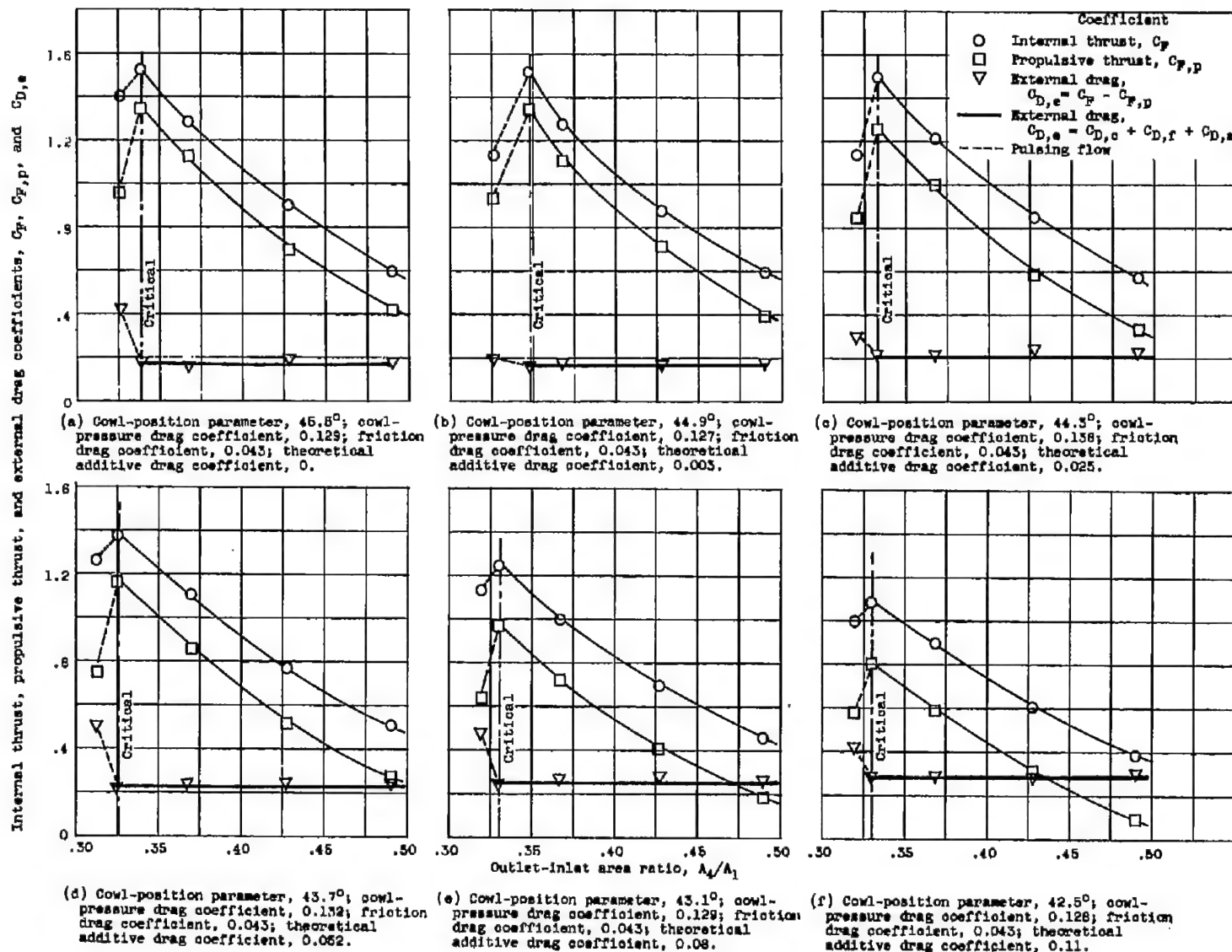


Figure 4. - Effect of position parameter on force data for one-cone inlet at zero angle of attack.

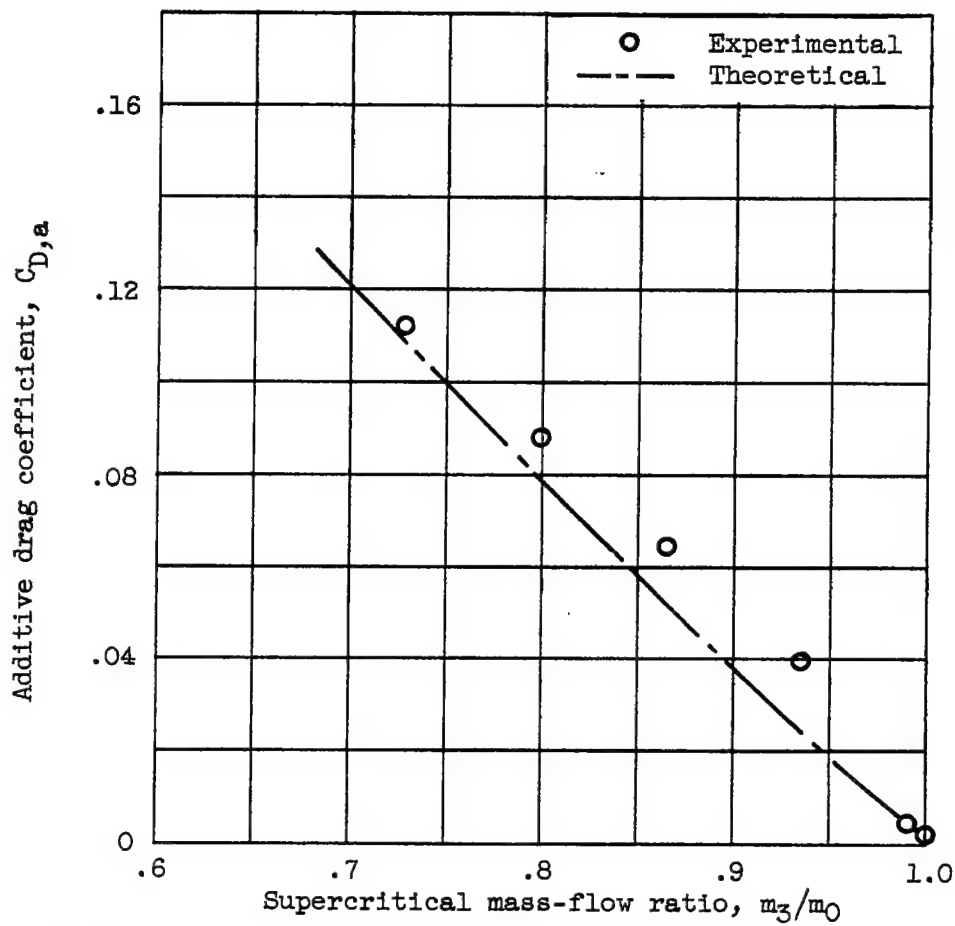


Figure 5. - Comparison of experimental and theoretical supersonic additive drags for one-cone inlet.

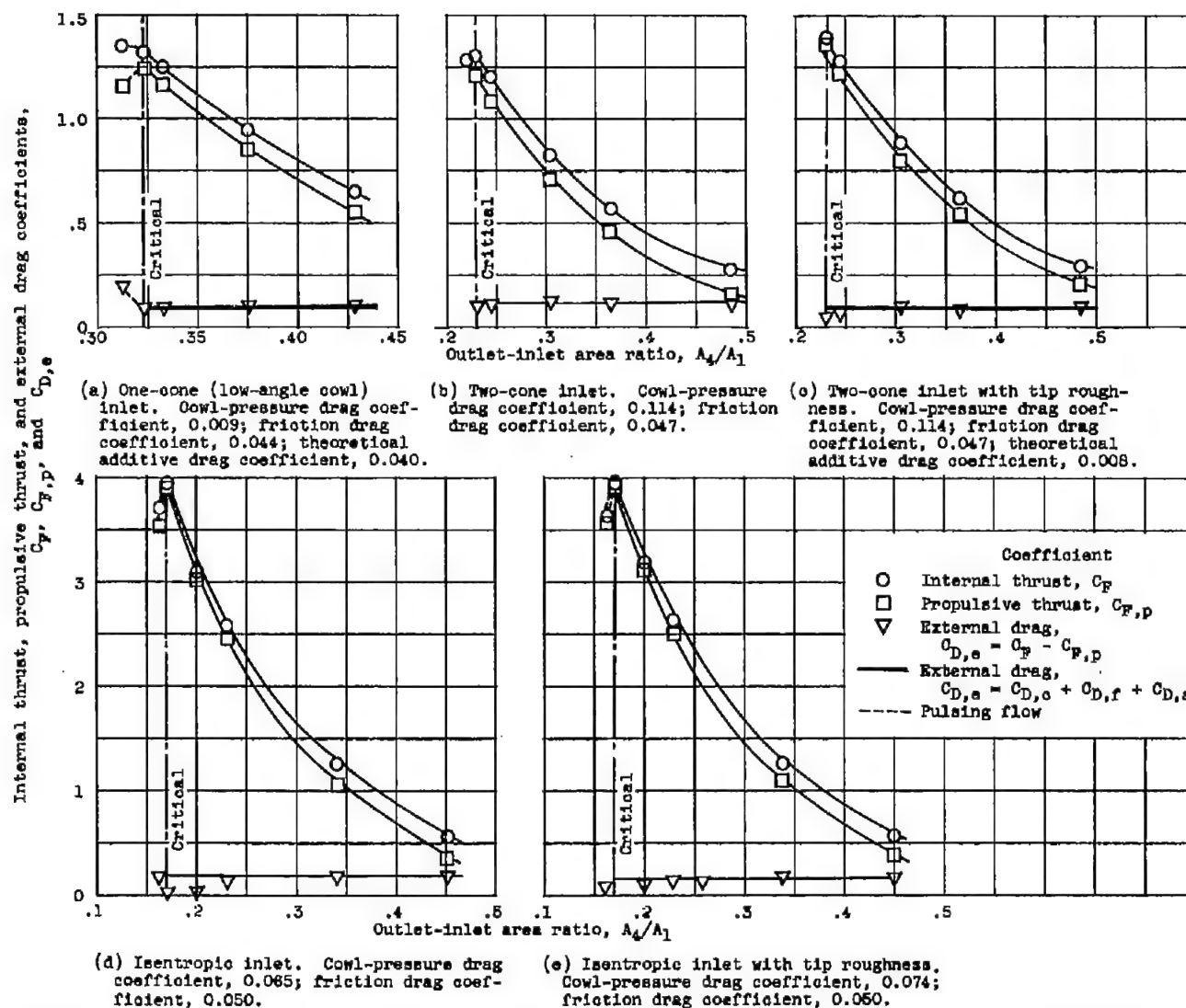


Figure 6. - Force data showing experimental external drag coefficients obtained for various inlet configurations at zero angle of attack.

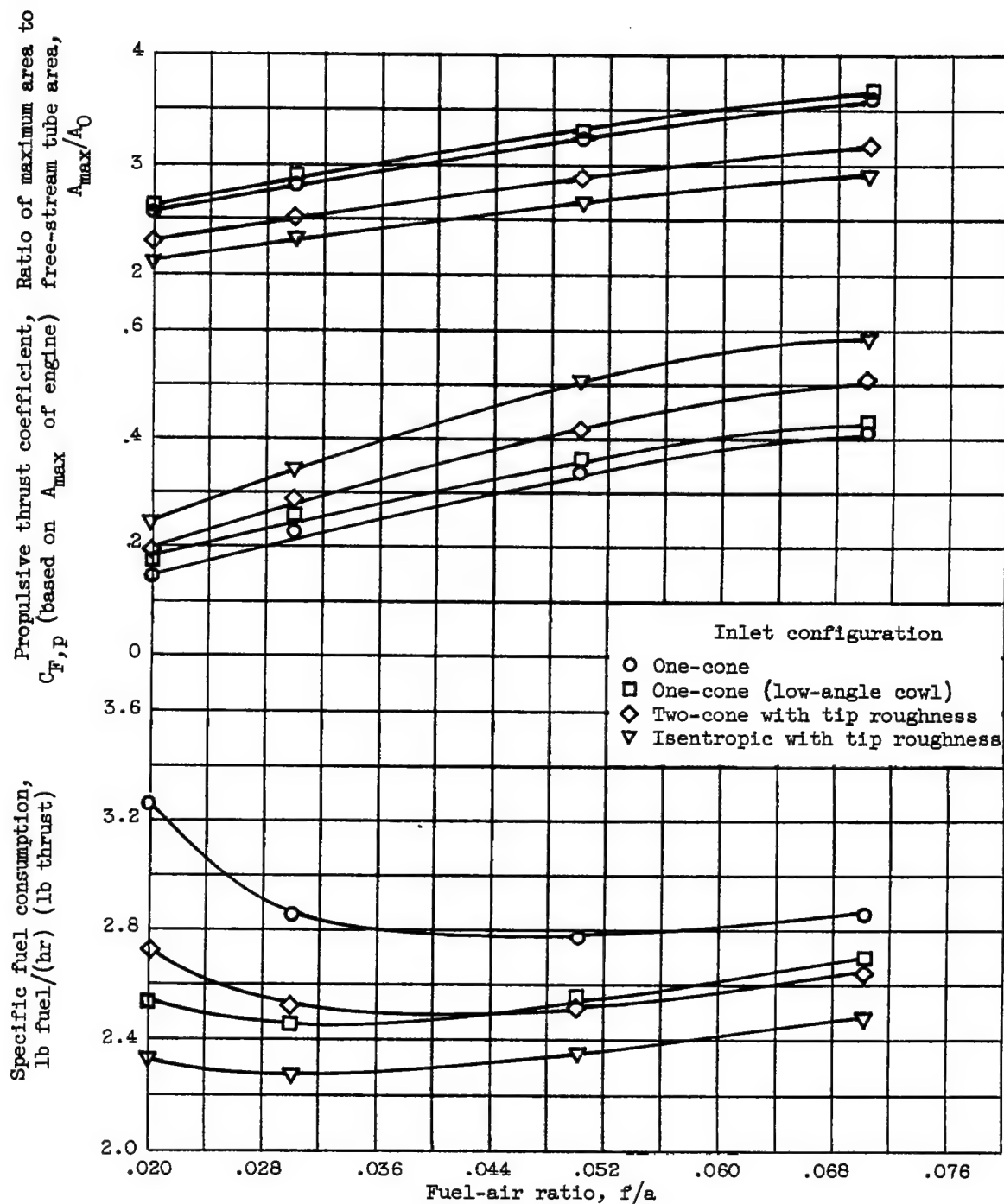
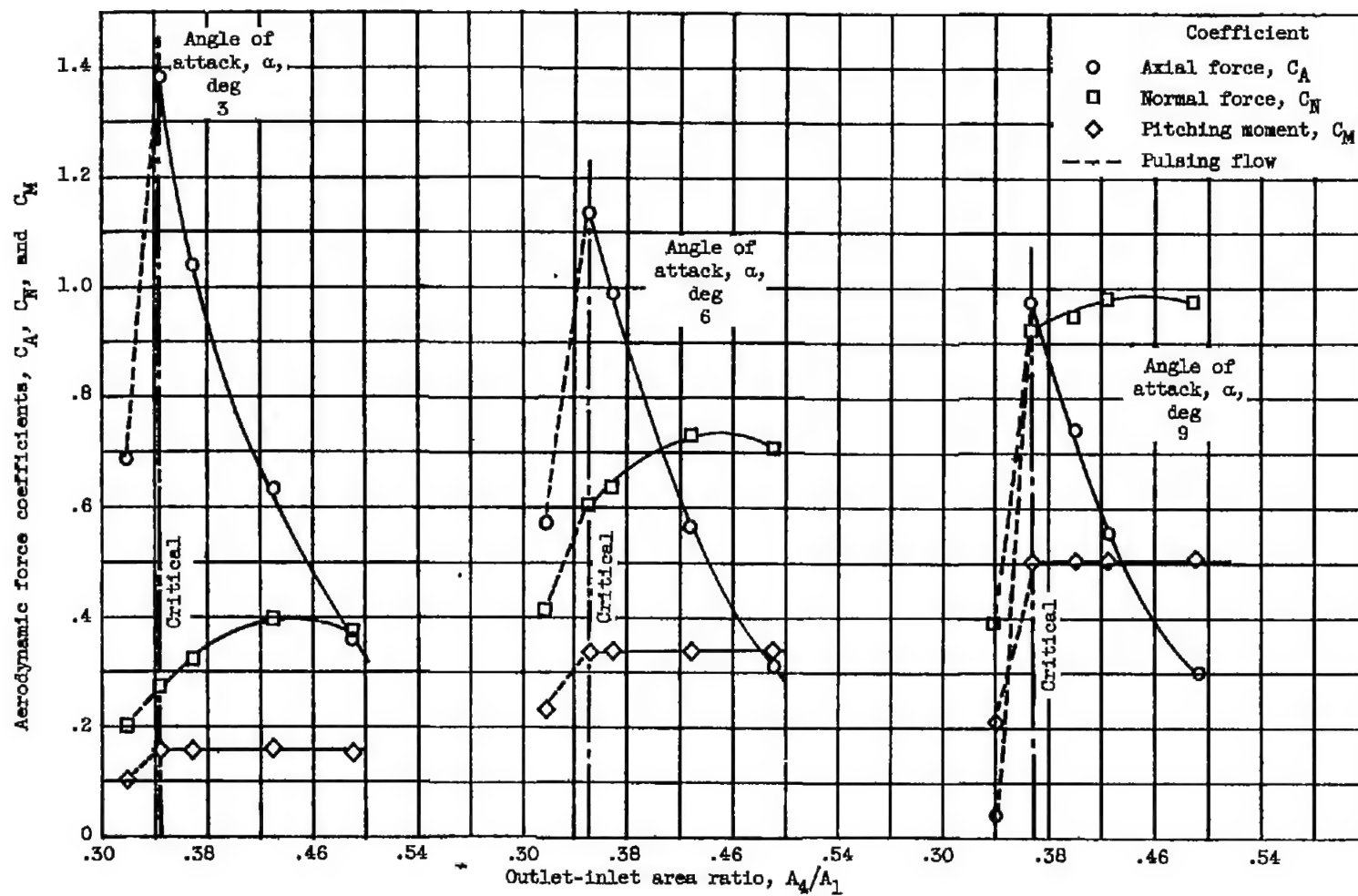
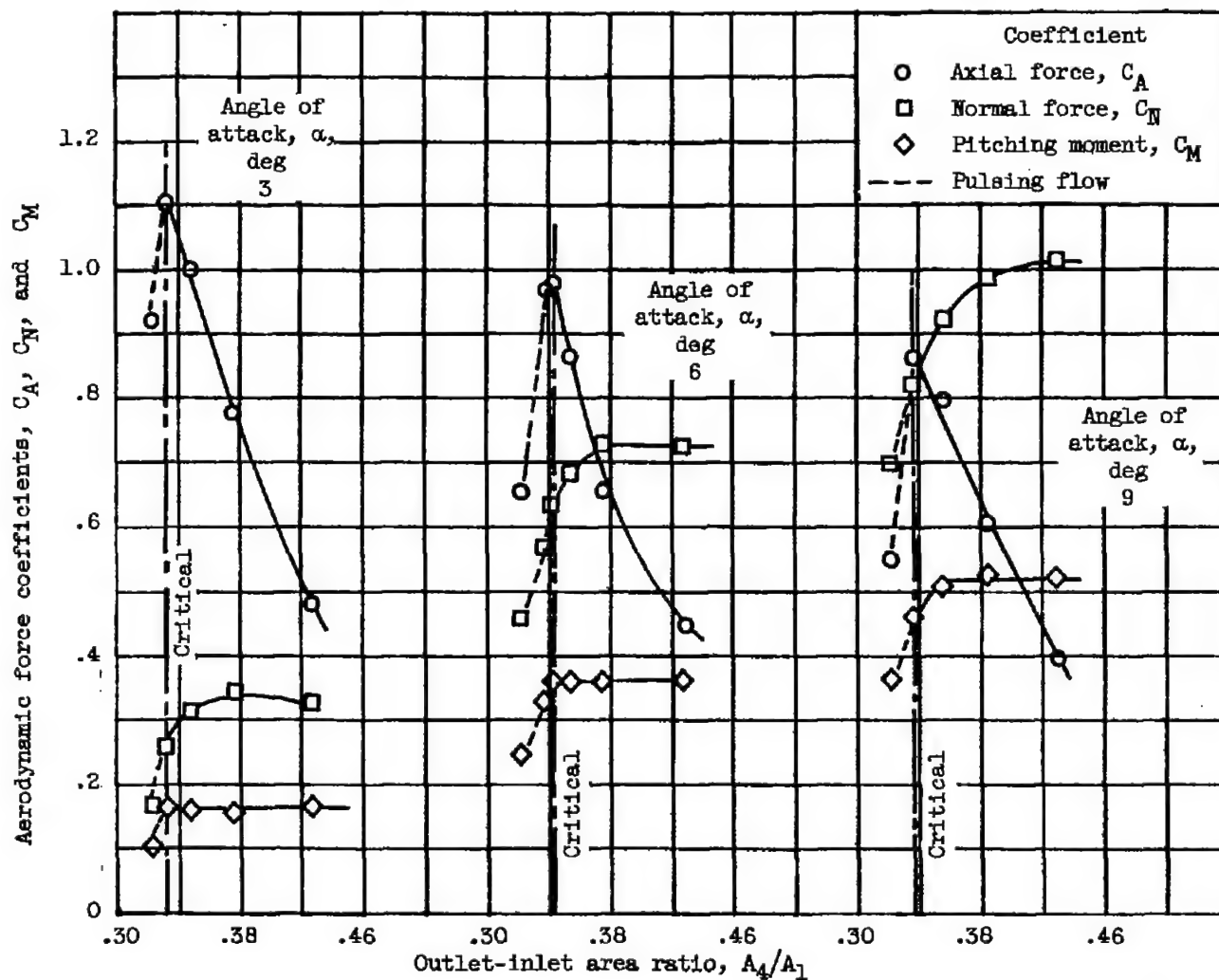


Figure 7. - Comparison of performance parameters for engines using various inlets and operating under following assumed conditions: free-stream Mach number, 3.85; altitude, 80,000 feet; combustion efficiency, 0.90; critical inlet operation; zero angle of attack; complete nozzle expansion.



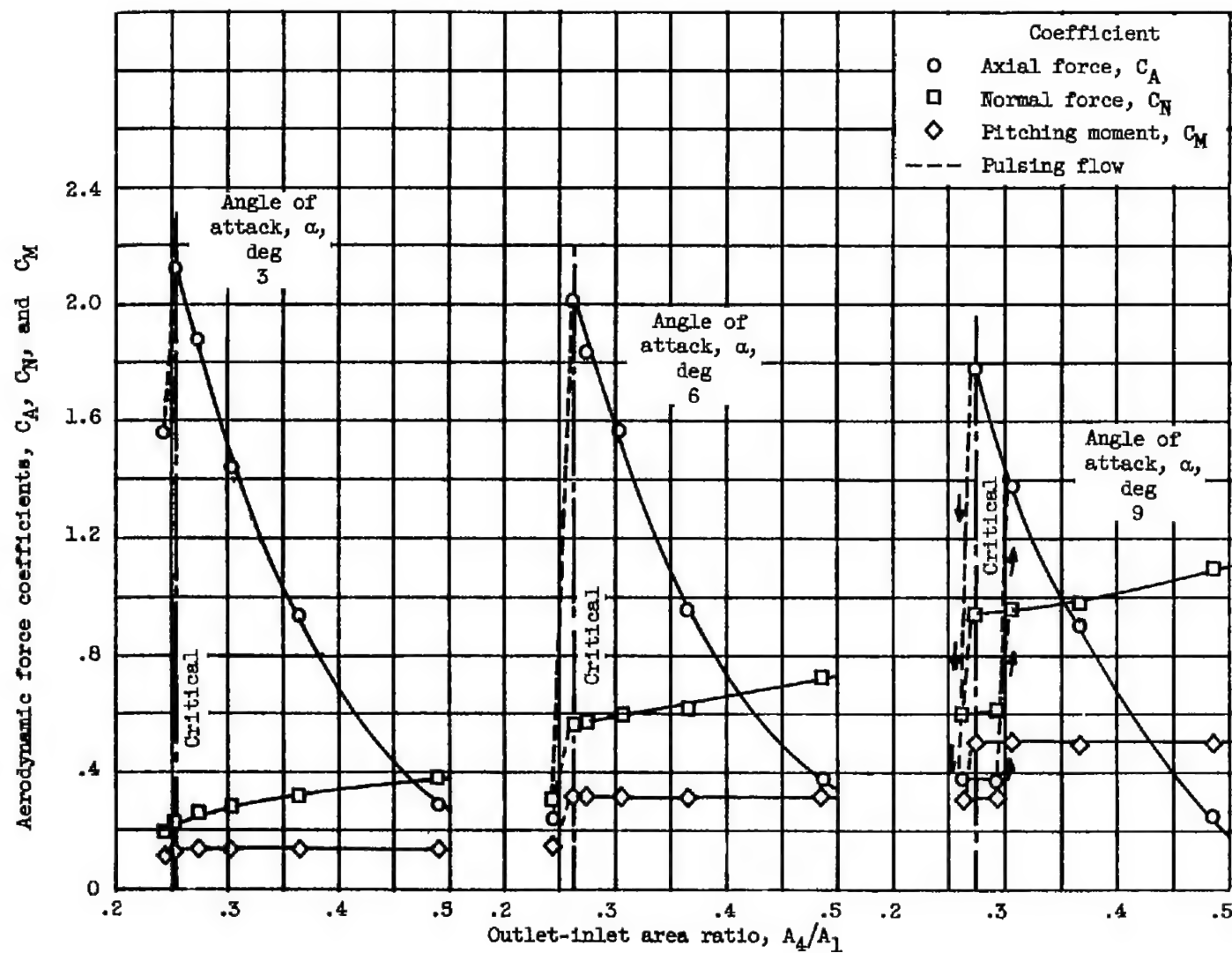
(a) One-cone inlet.

Figure 8. - Effect of angle of attack on aerodynamic force coefficients.



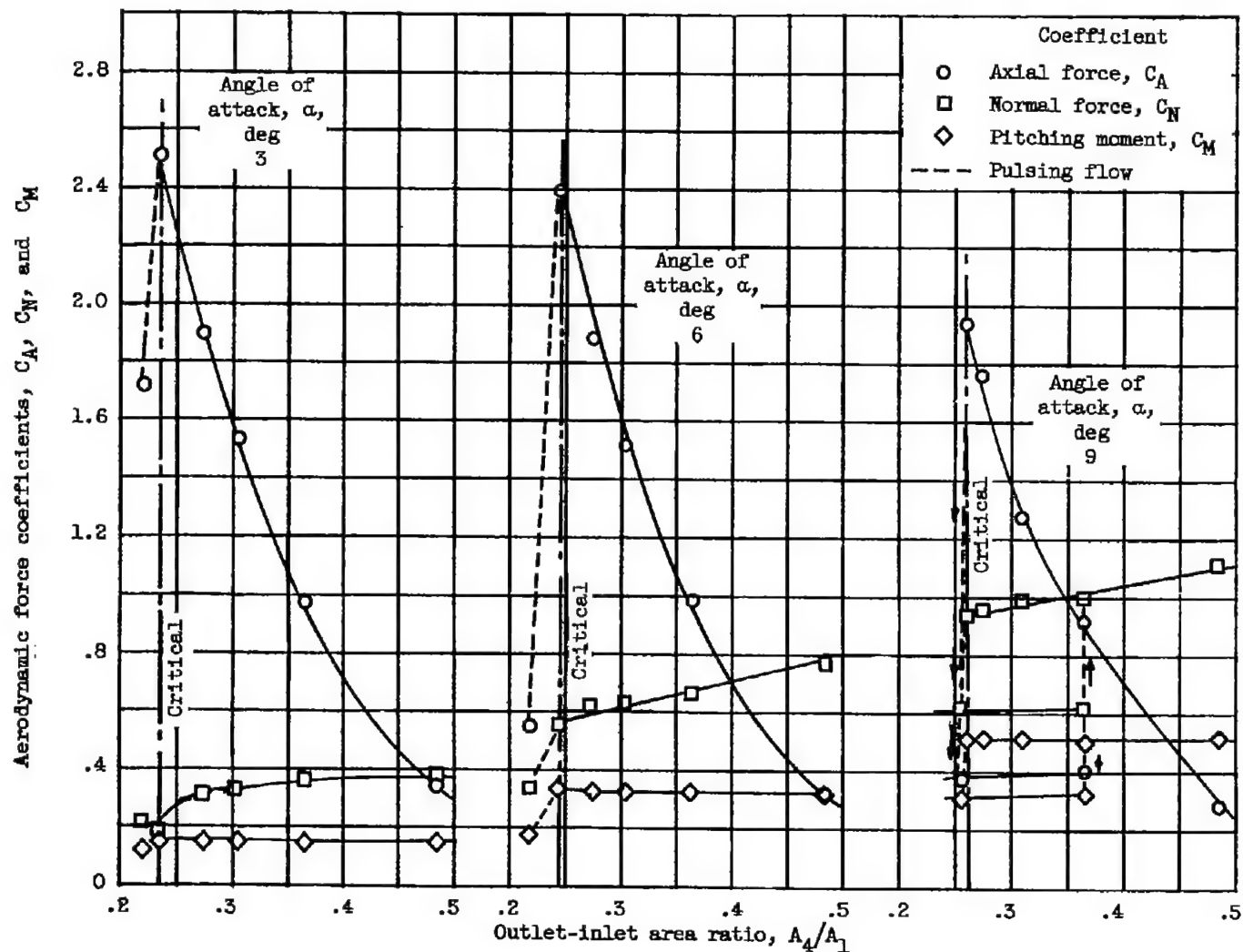
(b) One-cone (low-angle cowl) inlet.

Figure 8. - Continued. Effect of angle of attack on aerodynamic force coefficients.



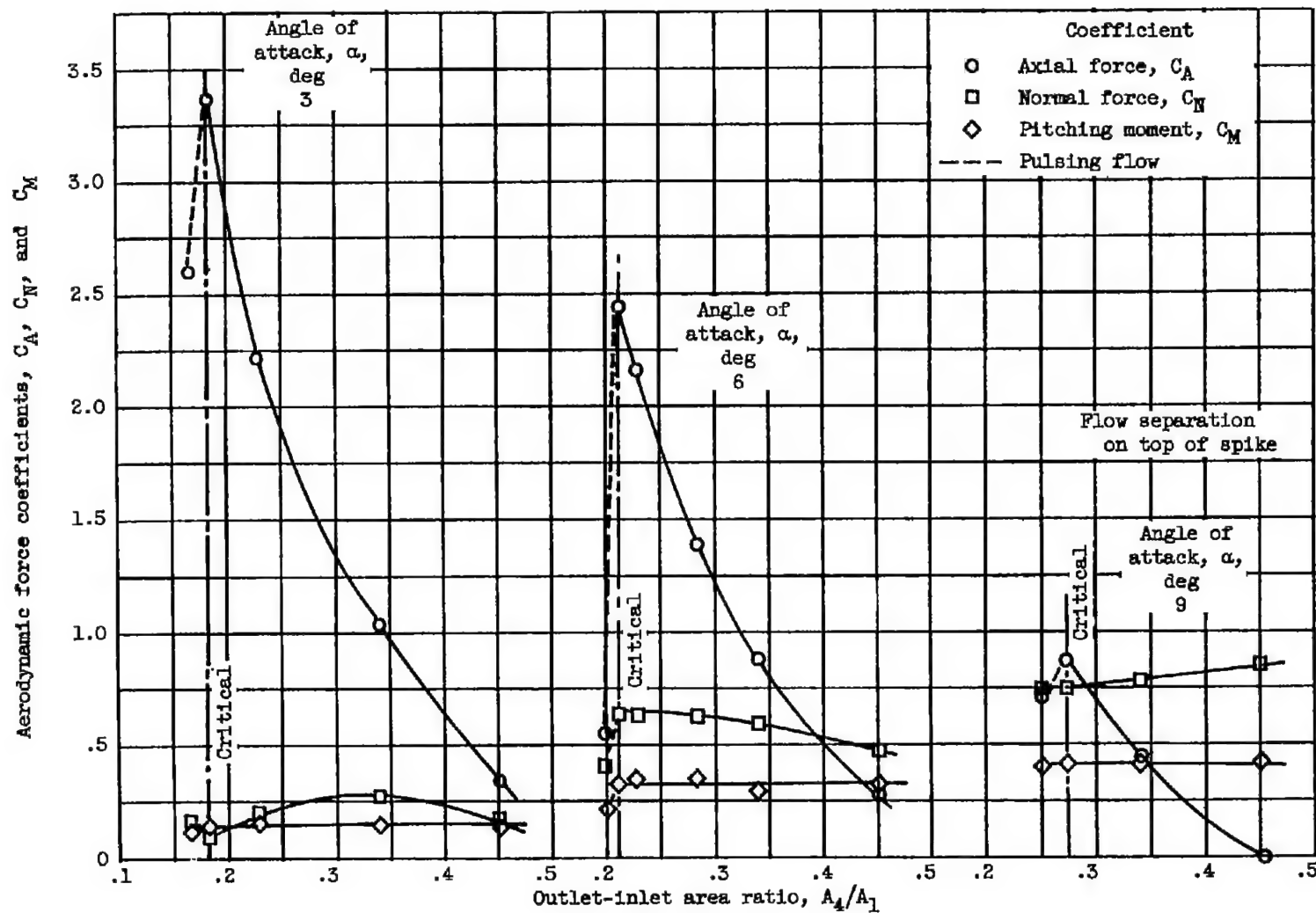
(c) Two-cone inlet.

Figure 8. - Continued. Effect of angle of attack on aerodynamic force coefficients.



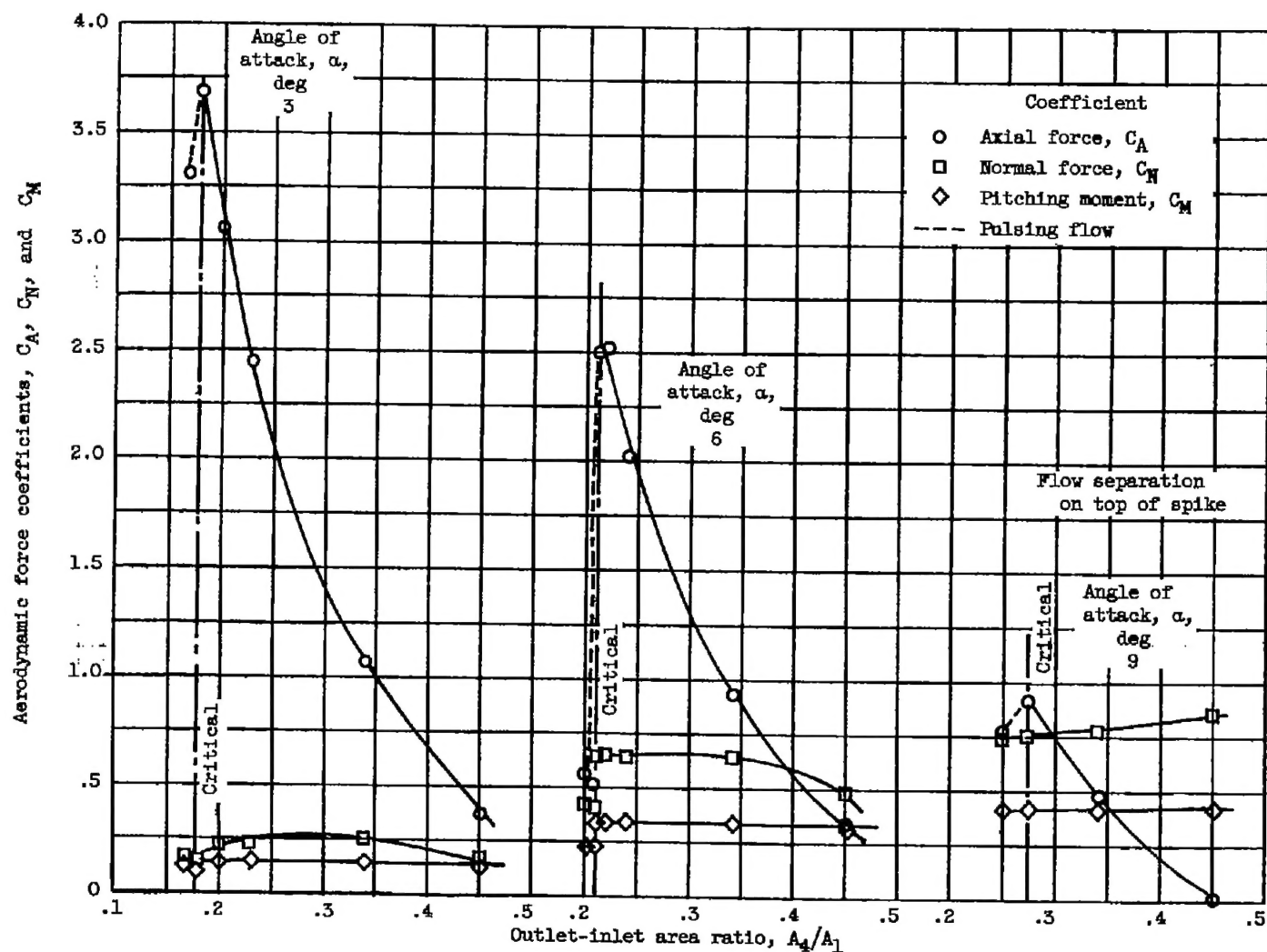
(d) Two-cone inlet with tip roughness.

Figure 8. - Continued. Effect of angle of attack on aerodynamic force coefficients.



(e) Isentropic inlet.

Figure 8. - Continued. Effect of angle of attack on aerodynamic force coefficients.



(f) Isentropic inlet with tip roughness.

Figure 8. - Concluded. Effect of angle of attack on aerodynamic force coefficients.

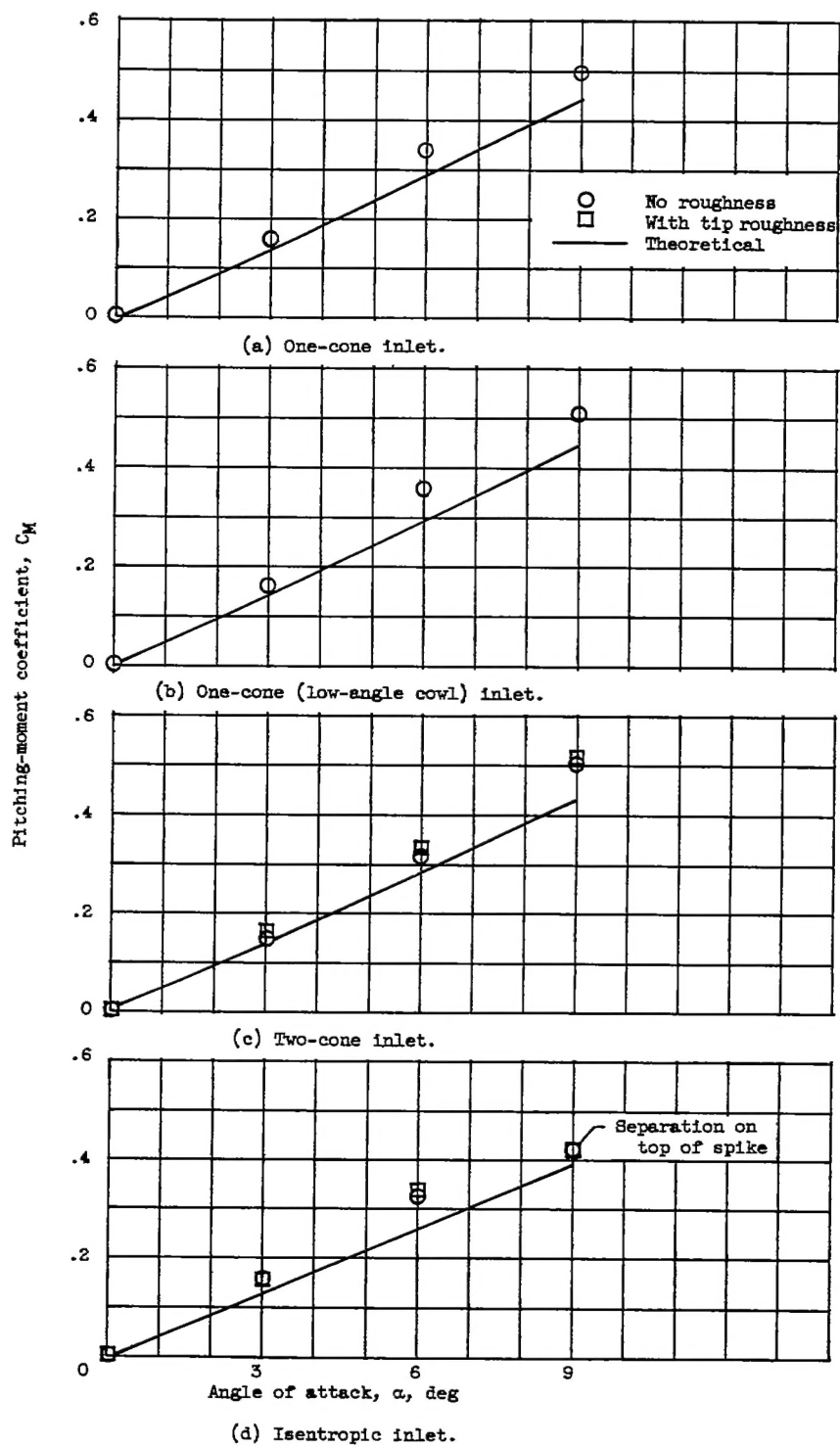


Figure 9. - Comparison of experimental and theoretical pitching-moment coefficients.

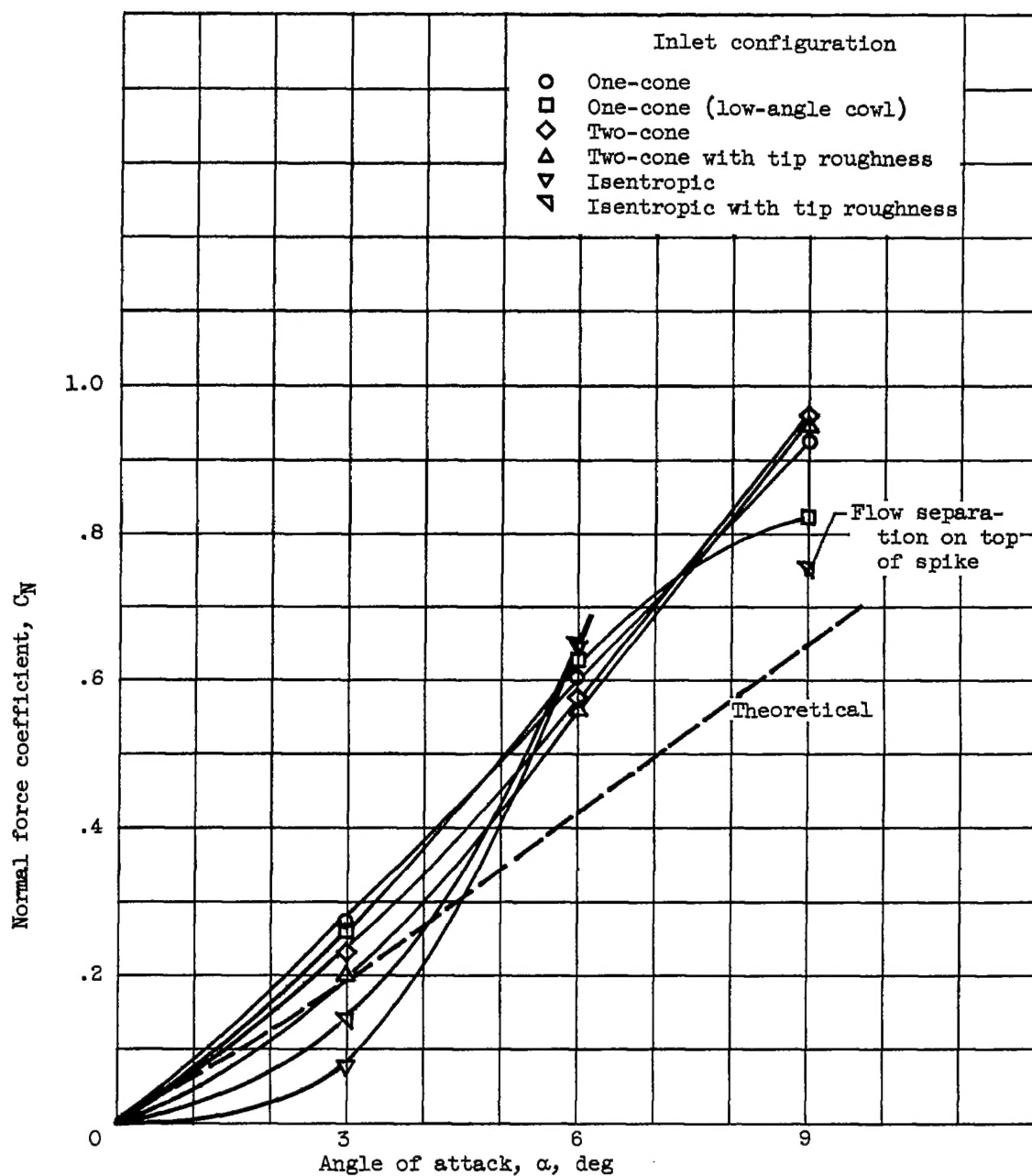


Figure 10. - Comparison of theoretical and experimental normal force coefficients during critical inlet operation.

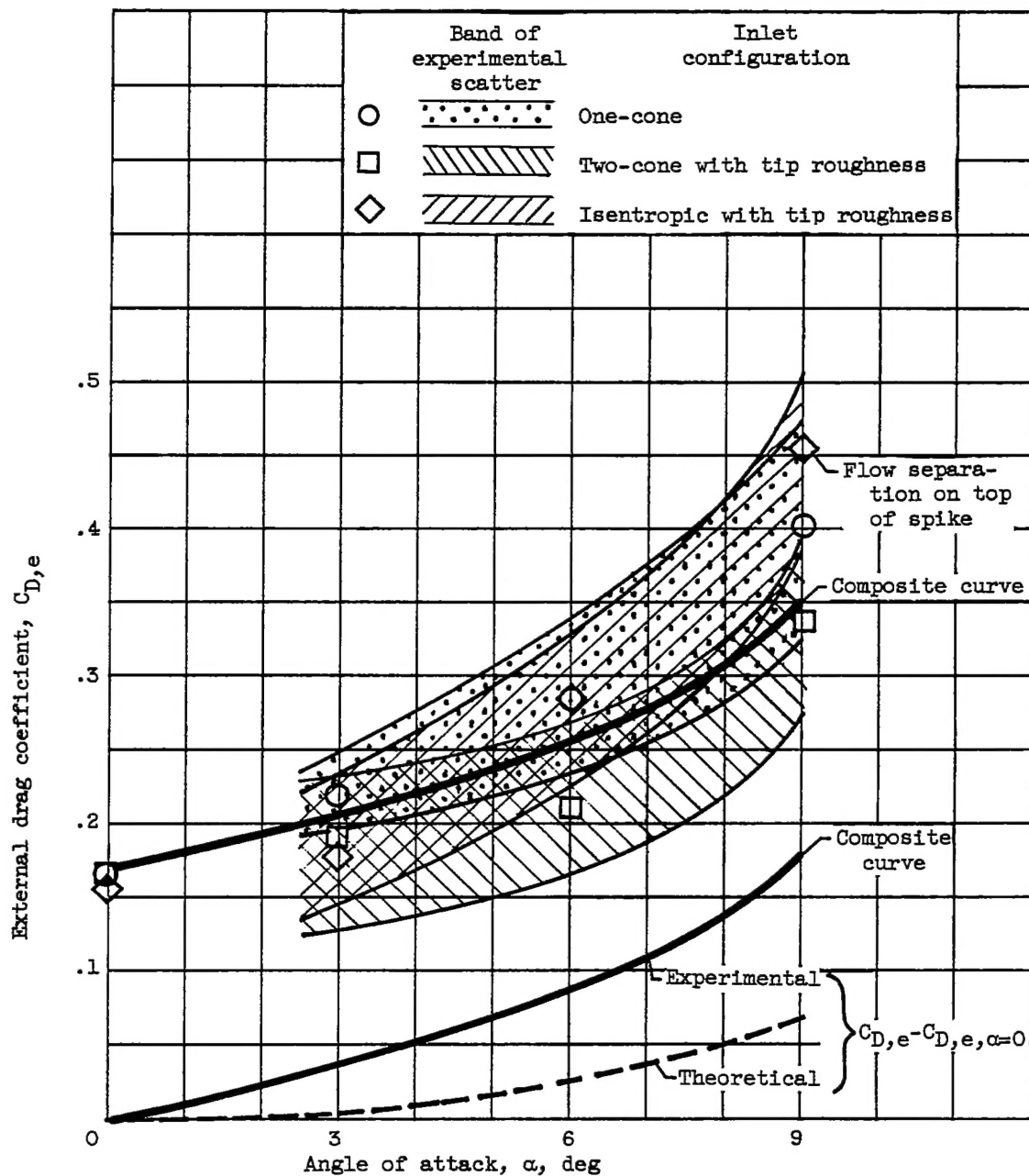


Figure 11. - Comparison of experimental and theoretical external drag coefficients.